

A Three-Dimensional Computational Model of PEM Fuel Cell with Serpentine Gas Channels

by

Phong Thanh Nguyen
B.E.Sc., University of Western Ontario, 2001

A Thesis Submitted in Partial Fulfillment of the Requirements for the Degree of

Master of Applied Science

in the Department of Mechanical Engineering

We accept this thesis as conforming to the required standard



Dr. N. Djilali, Supervisor (Department of Mechanical Engineering)



Dr. S. Dost, Department Member (Department of Mechanical Engineering)



Dr. H. Struchtrup, Department Member (Department of Mechanical Engineering)



Dr. M. A. Stuchly, External Examiner (Department of Electrical Engineering)

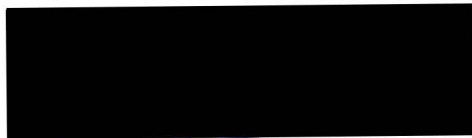
© PHONG THANH NGUYEN, 2003
University of Victoria

All rights reserved. This thesis may not be reproduced in whole or in part, by photocopy or other means, without permission of the author.

ABSTRACT

A three-dimensional computational fluid dynamics model of a Polymer Electrolyte Membrane (PEM) fuel cell with serpentine gas flow channels is presented in this thesis. This comprehensive model accounts for important transport phenomena in a fuel cell such as heat transfer, mass transfer, electrode kinetics, and potential fields. Results obtained from this model reveal the detailed transport phenomena occurring inside the fuel cell such as reactant gas distributions, temperature distribution, potential distribution, and local current density distribution. The unique feature of this model is the implementation of the voltage-to-current algorithm that solves for the potential fields which allows for the calculation of the local activation overpotentials. Hence, the accurate prediction of the local current density distribution is made possible through the coupling of activation overpotential distribution and reactant concentration distribution. The simulation results also reveal very different current distribution patterns for low and high load conditions, with current density maxima under the land area at low loading, and under the channel at higher loading. The validated model was also applied to investigate the sensitivity of several operating and electrode material properties on fuel cell performance.

Examiners:



Dr. N. Djilali, Supervisor (Department of Mechanical Engineering)



Dr. S. Dost, Department Member (Department of Mechanical Engineering)



Dr. H. Struchtrup, Department Member (Department of Mechanical Engineering)



Dr. M. Stuchly, External Examiner (Department of Electrical Engineering)

TABLE OF CONTENT

ABSTRACT	II
TABLE OF CONTENT	IV
LIST OF FIGURES	VIII
LIST OF TABLES	X
NOMENCLATURE	XI
1 INTRODUCTION	1
1.1 BACKGROUND	1
1.2 FUEL CELL COMPONENTS	2
<i>1.2.1 Polymer Electrolyte Membrane</i>	2
1.2.1.1 Membrane Molecular Structure	2
1.2.1.2 Membrane Morphology	3
<i>1.2.2 Gas Diffusion Layers</i>	6
<i>1.2.3 Catalyst Layer</i>	7
<i>1.2.4 Bipolar Plates</i>	7
1.3 LITERATURE REVIEW OF FUEL CELL MODELING.....	8
1.4 THESIS GOAL.....	12
2 FUEL CELL ELECTROCHEMISTRY	13
2.1 ELECTROCHEMICAL REACTIONS.....	13
2.2 GIBBS FREE ENERGY CHANGE IN FUEL CELL REACTIONS	13
2.3 ELECTRODE POTENTIAL	14

2.4	ELECTRODE KINETICS	16
2.5	OVER-POTENTIALS AND CROSSOVER LOSSES IN FUEL CELLS.....	16
2.5.1	<i>Internal Currents and Fuel Crossover</i>	17
2.5.2	<i>Ohmic Over-potential</i>	17
2.5.3	<i>Activation Over-potentials</i>	17
2.5.4	<i>Mass Transport Over-potential</i>	18
3	FUEL CELL MODEL	19
3.1	COMPUTATIONAL DOMAIN.....	19
3.2	MODELING EQUATIONS.....	20
3.2.1	<i>Flow in Gas Channels</i>	20
3.2.2	<i>Gas Diffusion Layers</i>	22
3.2.3	<i>Catalyst Layers</i>	23
3.2.4	<i>Membrane</i>	24
3.2.5	<i>Bipolar Plates</i>	25
3.3	POTENTIAL DROP ACROSS THE CELL	25
3.3.1	<i>Ohmic Loss in Gas Diffusion Layers</i>	25
3.3.2	<i>Ohmic Loss in Membrane</i>	26
3.3.3	<i>Activation Over-potential</i>	26
3.4	ELECTROCHEMICAL KINETICS	27
3.5	BOUNDARY CONDITIONS.....	28
3.5.1	<i>Inlets</i>	28
3.5.2	<i>Outlets</i>	29
3.5.3	<i>External Surfaces</i>	29

3.5.4	<i>Boundary Conditions at the Interfaces inside the Computational Domain ..</i>	29
3.6	COMPUTATIONAL PROCEDURE AND SOLUTION ALGORITHM.....	31
3.6.1	<i>Inner Iteration</i>	31
3.6.2	<i>Outer Iteration</i>	32
3.6.3	<i>Solution Algorithm</i>	33
3.7	MODELING PARAMETERS	35
4	MODEL VALIDATION AND RESULTS.....	40
4.1	MODEL VALIDATION	40
4.1.1	<i>Comparing with Experimental Data</i>	40
4.1.2	<i>Grid Study</i>	42
4.2	BASE CASE RESULTS AND DISCUSSIONS	43
4.2.1	<i>Velocity Profile</i>	43
4.2.2	<i>Oxygen Distribution</i>	44
4.2.3	<i>Hydrogen Distribution</i>	45
4.2.4	<i>Activation Overpotential Distribution in the Cathode Catalyst Layer</i>	45
4.2.5	<i>Current Density Distribution</i>	49
4.2.6	<i>Ohmic Overpotential</i>	52
4.2.7	<i>Membrane Overpotential</i>	52
4.2.8	<i>Water Distribution in the Cell</i>	55
4.2.9	<i>Cell Temperature Distribution</i>	55
4.2.10	<i>Analysis of the Turning Region</i>	57
5	PARAMETRIC STUDY.....	60

5.1	OPERATING PARAMETERS	60
5.1.1	<i>Effect of Temperature</i>	60
5.1.2	<i>Effect of Pressure</i>	66
5.2	DESIGN PARAMETERS AND MATERIAL PROPERTIES.....	69
5.2.1	<i>Effect of Electrode Porosity</i>	69
6	CONCLUSIONS AND RECOMMENDATIONS	71
6.1	CONCLUSIONS	71
6.2	CONTRIBUTIONS	72
6.3	RECOMMENDATIONS.....	72
	APPENDIX A	74
	MULTICOMPONENT DIFFUSION COEFFICIENT	74
	REFERENCES.....	78

List of Figures

Figure 1.1. Molecular structure of a tetra-fluoro-ethylene and sulfonyl vinyl ether monomer [Ref. [18]].	3
Figure 1.2. Morphology of membrane nanostructure [Ref. [21]].	5
Figure 1.3. Effect of membrane water content on pore structure [Ref. [18]].	6
Figure 3.1. Selection of computational domain	19
Figure 3.2. Computational domain.	19
Figure 3.3. Voltage-To-Current (VTC) algorithm.	34
Figure 4.1. Comparison of model and experimental polarization curves.	40
Figure 4.2. Comparison of model and experimental power density curves	41
Figure 4.3. Polarization curves comparing base case mesh and refined mesh results.	42
Figure 4.4. Velocity profile of the turning, inlet, and outlet regions in the cathode gas channel with a load of 1.2 A/cm^2 and $\text{Re} = 71.7$.	44
Figure 4.5. Oxygen molar fraction distribution in the cathode side for three loading conditions: 0.3 A/cm^2 (top), 0.69 A/cm^2 (middle), and 1.2 A/cm^2 (bottom).	46
Figure 4.6. Hydrogen molar fraction distribution in the anode side for three loading conditions: 0.3 A/cm^2 (top), 0.69 A/cm^2 (middle), and 1.2 A/cm^2 (bottom).	47
Figure 4.7. Activation overpotential distribution in the first catalyst layer for three loading conditions: 0.3 A/cm^2 (top), 0.69 A/cm^2 (middle), and 1.2 A/cm^2 (bottom).	48

Figure 4.8. Relative current density distribution for three loading conditions: 0.3 A/cm ² (top), 0.69 A/cm ² (middle), and 1.2 A/cm ² (bottom).....	50
Figure 4.9. 3-D view of current density distribution in the cathode catalyst layer for three loading conditions: 0.3 A/cm ² (top), 0.69 A/cm ² (middle), and 1.2 A/cm ² (bottom).	51
Figure 4.10. Ohmic overpotential in the cathode gas diffusion layer for three loading conditions: 0.3 A/cm ² (top), 0.69 A/cm ² (middle), and 1.2 A/cm ² (bottom). 53	
Figure 4.11. Potential drop across the membrane due to proton transport for three loading cases: 0.3 A/cm ² (top), 0.69 A/cm ² (middle), and 1.2 A/cm ² (bottom).	54
Figure 4.12. Water distribution in the cell for three different loading conditions: 0.3 A/cm ² (top), 0.69 A/cm ² (middle), and 1.2 A/cm ² (bottom); (RH = relative humidity).	56
Figure 4.13. Temperature distribution in the cell for two loading cases: 0.69 A/cm ² (top), and 1.2 A/cm ² (bottom).....	58
Figure 4.14. Distribution patterns at the turning region for the load of 1.2 A/cm ²	59
Figure 5.1. Fully humidified inlet air compositions at different temperatures.	64
Figure 5.2. Effect of temperature on fuel cell performance.	65
Figure 5.3. Fully humidified inlet air compositions at different pressures.....	66
Figure 5.4. Effect of pressure on fuel cell performance	68
Figure 5.5. Polarization curves illustrating the effect of electrode porosity on fuel cell performance.	70

List of Tables

Table 3.1	Difference scheme and linear equation solver used for each variable.....	32
Table 3.2	Cell dimensions for base case.....	35
Table 3.3	Operating conditions for base case.	36
Table 3.4	Electrode properties at base case conditions	37
Table 3.5.	Membrane properties	38
Table 3.6	Binary diffusivities at 1 atm.	39
Table 5.1.	Variation of exchange current density with temperatures at 3atm.	62
Table 5.2.	Variation of cell reversible potentials and membrane conductivity with temperatures.	63
Table 5.3.	Variation of exchange current density and reversible potential with pressures.	67

Nomenclature

Symbol	Description	Units
A_{MEA}	area of the MEA	cm^2
A_{ch}	cross sectional area of flow channel	cm^2
a	active surface per unit volume	$\text{cm}^2 \text{cm}^{-3}$
C_{H_2}	local hydrogen concentration	mol m^{-3}
$C_{\text{H}_2}^{\text{ref}}$	reference hydrogen concentration	mol m^{-3}
C_{O_2}	local oxygen concentration	mol m^{-3}
$C_{\text{O}_2}^{\text{ref}}$	reference oxygen concentration	mol m^{-3}
C_p	specific heat capacity	$\text{J kg}^{-1} \text{K}^{-1}$
D	diffusion coefficients	$\text{m}^2 \text{s}^{-1}$
E_{cell}	cell operating potential	volts
E_{rev}	reversible cell potential	volts
e	electronic charge	1.6022E-19 C
F	Faraday's constant	96487 C/mol
G	Gibb's free energy	J/mol
H	total enthalpy	J/kg
h	static enthalpy	J/kg
I	cell operating current density	A cm^{-2}
i_a	anode local current density	A cm^{-3}

i_c	cathode local current density	$A\text{ cm}^{-3}$
$i_{o,a}^{ref}$	anode reference exchange current density	$A\text{ cm}^{-3}$
$i_{o,c}^{ref}$	cathode reference exchange current density	$A\text{ m}^{-3}$
k_p	hydraulic permeability	m^2
L	channel length	m
M_{O_2}	molecular weight of oxygen	kg mol^{-1}
M_{H_2}	molecular weight of hydrogen	kg mol^{-1}
M_{H_2O}	molecular weight of water	kg mol^{-1}
N_w	net water flux across the membrane	$\text{kg m}^{-2}\text{ s}^{-1}$
n_e	number of electrons transfered	-
P	cell operating pressure	pa
\dot{q}	heat generation	W m^{-2}
R	universal gas constant	$8.314\text{ J mol}^{-1}\text{ K}^{-1}$
S	entropy	$\text{J mol}^{-1}\text{ K}^{-1}$
T	temperature	K
U	x-component of velocity	m s^{-1}
V	y-component of velocity	m s^{-1}
W	z-component of velocity	m s^{-1}
x_i	molar fraction	-
Y_i	mass fraction	-

Greek Symbols	Description	Units
α	charge transfer coefficient	-
ε	volume porosity	-
ϕ	any transport variable	-
γ	concentration parameter	-
η	overpotential	V
φ	any variable	-
λ_{eff}	effective electrode thermal conductivity	$\text{W m}^{-1} \text{K}^{-1}$
λ_{gr}	thermal conductivity of graphite	$\text{W m}^{-1} \text{K}^{-1}$
λ_e	electrode electronic conductivity	S m^{-1}
λ_m	membrane protonic conductivity	S m^{-1}
μ	chemical potential	J mol^{-1}
$\bar{\mu}$	electrochemical potential	J mol^{-1}
ρ	density	kg m^{-3}
ξ	stoichiometric flow ratio	-

1 INTRODUCTION

1.1 Background

Fuel cells are electrochemical energy conversion devices that convert directly the chemical energy of fuels through electrochemical reactions to electricity. Unlike batteries that are energy storage devices, fuel cells can operate continuously as long as fuel is supplied. The combination of high efficiency, environmental benefits, and versatility of fuel cells make them attractive alternative power conversion devices. The potential applications of fuel cells are very diverse ranging from a few watts for cell phones, laptops, to a few kilowatts for portable power generators, hundred kilowatts for cars and megawatts for large power generator. Despite many potential benefits, the commercial deployment of fuel cells still faces many challenges such as high cost and the lack of hydrogen infrastructures. Therefore the commercial viability of fuel cell technology is still to be established.

The classification of fuel cells is based on the electrolyte material. Some common types of electrolyte materials are proton exchange membrane (PEM), solid oxide, molten carbonate, potassium hydroxide (alkaline fuel cells), and phosphoric acid. In this category, PEM and solid oxide fuel cells have emerged as the most promising candidates for commercial applications. PEM fuel cells are in the focus of this thesis. The advantages of PEM fuel cells are low operating temperature, simplicity and versatility.

Many processes in PEM fuel cells are still not well understood. One approach to study fuel cell is through experimental techniques such as the ac impedance method where the impedance characteristics of the fuel cell can be investigated or the modes of failure can

be accessed. Other types of measurements that give polarization curves are also very useful in providing the operating characteristic of a fuel cell system. However, these experiments have limitation in revealing the detail of the transport phenomena occurring inside the fuel cell. This is where computational fluid dynamics (CFD) modeling can be a great complement to experimental techniques. The physical transport phenomena and electrode kinetics inside the fuel cell can be modeled and solved using numerical methods.

1.2 Fuel Cell Components

1.2.1 Polymer Electrolyte Membrane

The Polymer electrolyte membrane (PEM) is probably the most complex and sensitive component of the PEMFC. The characteristics of the membrane have direct influence on the performance of PEMFC, therefore the membrane deserves a more detailed discussion than other components. At the core of a PEMFC is the polymer electrolyte membrane that separates the anode from the cathode. The desired characteristics of PEMs are high proton conductivity, good electronic insulation, good separation of fuel in the anode side from oxygen in the cathode side, high chemical and thermal stability, and low production cost [13]. One type of PEMs that meets most of these requirements is Nafion. This is why Nafion is the most commonly used and investigated PEM in fuel cells.

1.2.1.1 Membrane Molecular Structure

The Nafion membrane belongs to a class of poly-perfluoro-sulfonic acids which consists of a hydrophobic tetrafluoroethylene backbone with pendant side chains of perfluorinated vinyl-ethers terminated by sulfonic acid groups [18]. The precursor of

Nafion is a copolymer of tetrafluoroethylene and a sulfonyl vinyl ether with a molecular formula as shown in Figure 1.1.

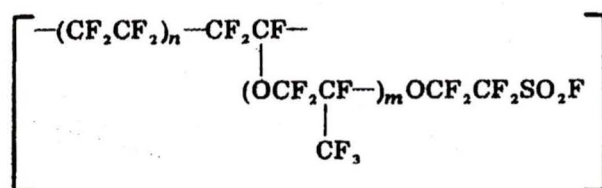


Figure 1.1. Molecular structure of a tetra-fluoro-ethylene and sulfonyl vinyl ether monomer [Ref. [18]].

Here the value of m can be as low as 1 and n ranges between 6 and 13. The sulfonyl fluoride group is easily hydrolyzed to form the strongly acidic sulfonic acid ion exchange site.

1.2.1.2 Membrane Morphology

Perfluoro-sulfonate polymers typically have ordered structures where the hydrophilic end groups aggregate within the hydrophobic matrix composed of the fluorocarbon backbone of the polymer [18]. Ion clustering in Nafion has been suggested by a number of techniques including mechanical and dielectric relaxation, NMR, IR, electron microscopy and X-ray studies. Probably the most direct evidence comes from the small-angle X-ray diffraction technique. Many models have been proposed to describe the structural organization of the perfluoro-sulfonate polymers. However, no single accepted view of membrane structure has emerged. Probably, no simple geometry will give an appropriate description. Instead, it is most likely that the water fractions can be considered to form tortuous pathways with ramified boundaries. Nonetheless, this highly interconnected

porous structure may be subdivided, at least for model purposes, into elementary segments resembling cylinders or spheres.

A widely accepted model of PEM morphology is due to Gierke [18] who proposed an inverted micellar structure (Figure 1.2) in which the ionic clusters exist as an interconnected, spherical pore network. This model is based on experimental measurements obtained from wide-angle X-ray and small-angle X-ray of Nafion membrane. In this model, the polymeric ions and absorbed water separate from the fluorocarbon matrix into approximately spherical domains connected by short narrow channels. Such a structure satisfies the strong tendency for the sulfonic acid sites to be hydrated, and at the same time this structure will minimize unfavorable interactions between water and the fluorocarbon matrix. The distance between the clusters can be obtained from small angle X-ray data, and the cluster diameter can be deduced from the water absorption data. In this paper [18], they also found that ion transport in Nafion perfluorinated membrane is controlled by percolation, which means that the connectivity of ion-clusters is critical. This reflects the heterogeneous nature of a wet Nafion membrane and supports the cluster-network model.

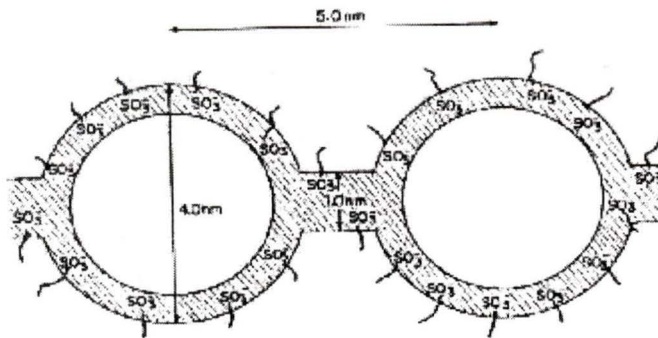


Figure 1.2. Morphology of membrane nanostructure [Ref. [21]].

An average pore in the swollen state has a diameter of 4-5 nm and contains approximately 70 fixed SO_3^- groups sitting at the inner pore surface with a spacing of about 1nm, and is filled with approximately 1000 water molecules. As the polymer absorbs more water, the cluster diameter, number of exchange sites per cluster, and number of water molecules per exchange site all increase. The increase in the number of exchange sites per cluster with increasing water content is noteworthy because it suggests that cluster growth does not merely occur by an expansion of the dehydrated cluster. Rather, the growth of clusters appears to occur by a combination of this expansion and a continuous reorganization of exchange sites between clusters so there are actually fewer clusters in the fully hydrated sample. Figure 1.3 shows the exchange sites from two clusters could be redistributed to form a third new cluster without significant spatial translation of the polymer chains.

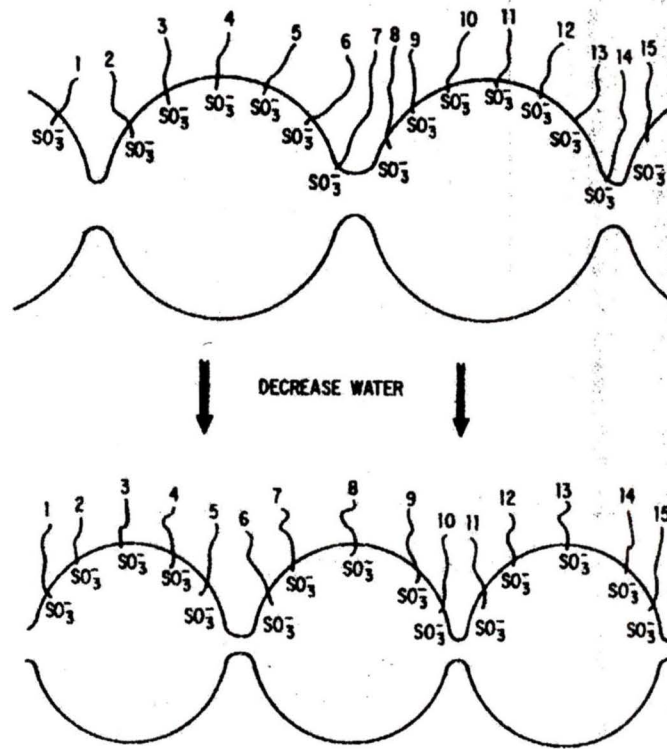


Figure 1.3. Effect of membrane water content on pore structure [Ref. [18]].

1.2.2 Gas Diffusion Layers

The typical materials for gas diffusion layers are carbon paper and carbon cloth. These are porous materials with typical thickness of 100-300 μm [27]. The functions of the gas diffusion layers are to provide structural support for the catalyst layers, passages for reactant gases to reach the catalyst layers and transport of water to or from the catalyst layers, electron transport from the catalyst layer to the bipolar plate in the anode side and from the bipolar plate to the catalyst layer in the cathode side, and heat removal from the

catalyst layers. Gas diffusion layers are usually coated with Teflon to reduce flooding which can significantly reduce fuel cell performance due to poor reactant gas transport.

1.2.3 Catalyst Layer

The best catalyst material for both anode and cathode PEM fuel cell is platinum. Since the catalytic activity occurs on the surface of the platinum particles, it is desirable to maximize the surface area of the platinum particles. A common procedure for surface maximization is to deposit the platinum particles on larger carbon black particles [25]. Several methods of applying the catalyst layer to the gas diffusion electrode have been reported. These methods are spreading, spraying, and catalyst power deposition. For the spreading method, a mixture of carbon support catalyst and electrolyte is spread on the GDL surface by rolling a metal cylinder on its surface [27]. In the spraying method, the catalyst and electrolyte mixture is repeatedly sprayed onto the GDL surface until a desired thickness is achieved. A common problem of the anode catalyst is CO poisoning. Since platinum has a strong affinity for CO and CO exists in very small amount in the common reformed hydrogen fuel. Doping platinum with ruthenium has been shown to reduce the effect of CO poisoning [27].

1.2.4 Bipolar Plates

The functions of the bipolar plate are to provide the pathways for reactant gas transport, and electron conduction paths from one cell to another in the fuel cell stack, separate the individual cells in the stack, carry water away from the cells, and provide cooling passages. Plate material and topologies facilitate these functions. Common plate

topologies are straight, serpentine, or inter-digitated flow fields. Desirable material characteristics of bipolar plates are high electrical conductivity, impermeability to gases, good thermal conductivity, light weight, high corrosion resistance, and easy to manufacture. The common materials used in bipolar plates are graphite, metals such as stainless steel, aluminum, or composite materials [27]. Graphite plates meet most of the requirements for optimal fuel cell performance, however the disadvantage of graphite plates is the high cost of machining the flow fields. Metallic plates are cheap and easy to manufacture, but they have high contact resistance due to the metal oxide layer forming between the plate and the gas diffusion layer. Metallic plates also suffer high degradation from the corrosive fuel cell environment that leads to short life cycles. However, some coated metallic plates have been shown to produce performance comparable to graphite plates. Finally, composite plates can offer the combined advantages of high electrical and thermal conductivity of graphite plates and low manufacturing cost of metallic plates [1].

1.3 Literature Review of Fuel Cell Modeling

The transport phenomena of chemical species in PEM fuel cell are difficult to observe and measure by experiments. Computational modeling is a good alternative approach in the study of fuel cell performance relating to the transport processes and electrochemical reactions. In the early 1990s, most models were one dimensional, isothermal and focusing on the electrode, catalyst layer and membrane. Towards the late 1990s, the models are more advanced and including multi-dimensionality (2-D or 3D) and multiphase flow. However, a complete model that takes into account all aspects of

species transport and electrochemical reactions are yet to be achieved. Illustrated below is a brief overview of the modeling strategies employed by some of the models reported in the literature. Some of these modeling approaches were used in this work.

One of the pioneer fuel cell models addressing water management and species transport in the gas diffusion layer was developed by Bernardi et al. [2] in 1991. This one-dimensional (1-D) computational domain consists of cathode gas channel and gas diffusion layer attached to the membrane. Some of the important assumptions used in this model are isothermal, steady state, ideal gases. Mass transport in the gas channel is modeled by the Stefan-Maxwell equations which solve for the mass fractions of oxygen, water vapor, and nitrogen. Transport in the gas diffusion layer is modeled as transport in porous medium where the diffusivities are corrected with the Bruggeman correction equation. Nernst-Planck equation is used for modeling the transport of protons across the membrane. Protons are transported by potential gradient, concentration gradient, and convection effect. The membrane is assumed electroneutral where the total charge of protons is equal to the total charge of the negative sulfonate groups. The Butler-Volmer equation is used to model the electrode kinetics in the active catalyst layer. The analysis of this model focused on polarization characteristics, water transport, and catalyst utilization. As an extension to the previous model, in 1992, Bernardi et al. [3] published a complete model with both anode and cathode sides. The governing equations in this model are the same as those in the last model. In this model the authors focus on the calculations of the activation overpotential, membrane resistance loss, and ohmic loss in the gas diffusion layers due to electron transport. Anode activation is also accounted for in this model. Overall, the electrochemical treatments in this model are very

comprehensive. However, the drawbacks of this model are its limitation of one dimensionality and isothermal assumption.

Springer is another pioneer in fuel cell modeling. In 1991, Springer et al. [37] presented an isothermal, one-dimensional, steady state model for a PEM fuel cell with a hydrated Nafion-117 membrane. The unique feature of this model is the empirical relation for calculating membrane conductivity based on water content in the membrane. Also, membrane water content at the interface is determined by the activity of water vapor at the electrode/membrane interface. The electro-osmotic drag coefficient, i.e. the ratio of number of water molecules transported across the membrane per proton, is also calculated based on the water content of the membrane. The cell potential is calculated based on a given load current.

In 1993, Nguyen et al. [29] presented a steady state, two-dimensional heat and mass transfer model. The model computational domain consists of the typical regions such as gas flow channels, gas diffusion layers, catalyst layers, and membrane. This model accounts for mass transport of water across the membrane by electro-osmosis and diffusion, heat transfer from the solid phase to the gas along the flow channels. The electro-osmotic drag coefficient of water across the membrane is calculated based on the empirical relations of water vapor pressure activities given by Springer et al. [37]. The net water flux from across the membrane is calculated as the difference between electro-osmotic drag and back diffusion from the cathode to the anode. Cell potential is calculated as the difference between open circuit potential and activation overpotential loss and ohmic loss in the membrane. This model accounts for varying activation overpotential as a function of local current density and oxygen partial pressure. The

solution algorithm in this model starts with the specification of a load current, then a guessed voltage is used to calculate the local current densities, the procedure is repeated until the guessed voltage produce a current correspond to the input current.

In 1998, Gurau et al. [20] applied computational fluid dynamics to fuel cell modeling where they began with a two-dimensional model consisting of both the anode and cathode sides. This model fully accounted for the mass transport of reactant species which have been simplified in earlier models. The application of CFD to fuel cell modeling has resulted in several advanced models that are three-dimensional and two phase [4], [41].

The previous model at IESVIC focused on the single phase and multiphase flows in straight channel was developed by Berning [4]. In particular, the single-phase model accounts for many important transport phenomena in a complete assembly of gas channels, porous gas diffusion electrodes, and thin catalyst layers. Heat transfer is also considered in this model. The physical structure of the fuel cell is split into four computational domains in this model. The main computational domain accounts for gas flow, heat and mass transfer inside the flow channels and gas diffusion electrodes. Subdomain I consists of the MEA, Subdomain II also consists of the MEA and is used for solving liquid water flux through the membrane. Subdomain III consists of the membrane only and is used for calculating the electric potential drop. In this model, the electrode kinetic is modeled by a simplified version of the Butler-Volmer equation which only accounts for the dependence of current density on oxygen concentrations. This is one of the major limitations of this modeling approach.

Most CFD based models presented to date do not resolve the three-dimensional nature of the catalyst layer and use simplified electrochemical kinetics in which constant activation overpotential is assumed. In addition, there is only one model reported by Dutta et al. [12], which investigates the effects of serpentine flow field design. However, many current fuel cell flow field designs use serpentine flow channels. Therefore, it is important to include serpentine channel in the modeling of fuel cell transport phenomena and performance.

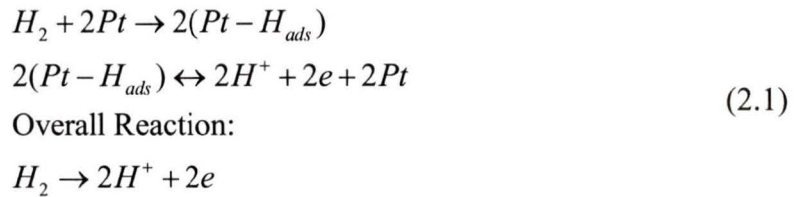
1.4 Thesis Goal

The goal of this thesis is to develop a comprehensive three-dimensional model that accounts for all important transport phenomena and electrochemical kinetics in the fuel cells with serpentine gas flow channels. A new algorithm for predicting the cell current based on a given cell voltage is also developed in this model. The results obtained from this model will be validated with experimental results and the fully validated model is used in a series of parametric studies to investigate the sensitivity of various operating and design parameters on fuel cell performance.

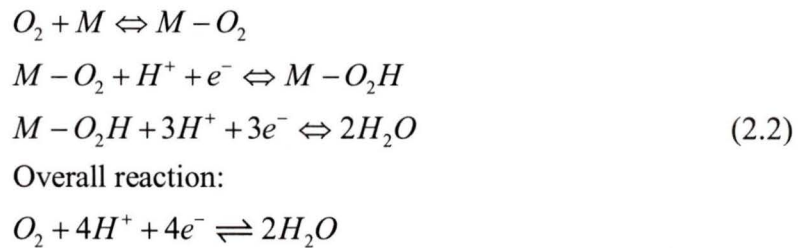
2 FUEL CELL ELECTROCHEMISTRY

2.1 Electrochemical Reactions

At the anode catalyst layer, hydrogen is oxidized to protons on platinum catalyst surface based on the following mechanism,



At the cathode side oxygen is reduced to water in presence of protons, electrons on platinum catalyst surface. This reaction mechanism is more complicated and less understood. This is a multi-step, multi-species reaction, which is very difficult to characterize in terms of electrochemistry. The proposed mechanism [34], is below,



Here M is the catalyst metal.

2.2 Gibbs Free Energy Change in Fuel Cell Reactions

Fuel cell electrochemical reactions convert free energy change associated with the chemical reaction into electrical energy directly. The Gibbs free energy change in a chemical reaction is a measure of the maximum net work obtainable from a chemical reaction.

$$\Delta g = \Delta h - T\Delta s \tag{2.3}$$

The basic thermodynamic functions are internal energy U , enthalpy H , entropy S , and Gibbs free energy G . These are extensive properties of a thermodynamic system and they are first order homogenous functions of the components of the system. Pressure and temperature are intensive properties of the system and they are zero-order homogenous functions of the components of the system. Electrochemical potentials are the driving force in an electrochemical system. The electrochemical potential comprises chemical potential and electrostatic potential in the following relation.

Chemical potential:

$$\mu_i = \left(\frac{\partial G}{\partial N_i} \right)_{T,P,N_j} \quad (2.4)$$

Electrochemical potential:

$$\bar{\mu}_i = \mu_i + zF\phi \quad (2.5)$$

where μ_i is the chemical potential, z is the charge number of the ion, ϕ is the potential at the location of the particles i .

2.3 Electrode Potential

The reversible electrode potential of a chemical reaction can be obtained from the Nernst equation,

$$E_{rev} = E^o - \frac{RT}{nF} \ln \left(\frac{\sum_i a_i^{v_i}}{\sum_j a_j^{v_j}} \right) \quad (2.6)$$

Where E^o is the reversible potential at standard state, a_i and a_j are activity coefficients of the products and reactants respectively, v_i and v_j are the stoichiometric coefficients

respectively. The standard state reversible electrode potential can be calculated from the thermodynamic property of standard Gibbs free energy change of the reaction as,

$$E^o = -\frac{\Delta G^o}{nF} \quad (2.7)$$

It can be seen from these relations that the reversible potential is dependent on temperature and pressure since the Gibbs free energy is a function of temperature and the activity coefficients are dependent on temperature, pressure for gases and ionic strengths for ionic electrolytes. The Nernst equation (2.6) is used to derive a formula for calculating the reversible cell potential as follows:

Anode electrode potential,

$$E_a = E_a^o + \frac{RT}{2F} \ln \left(\frac{a_{H^+}^2}{a_{H_2}} \right) \quad (2.8)$$

Cathode electrode potential:

$$E_c = E_c^o - \frac{RT}{2F} \ln \left(\frac{a_{H_2O(g)}}{a_{H^+}^2 a_{O_2}^{1/2}} \right) \quad (2.9)$$

The absolute electrode potential of the fuel cell is difficult to measure. However, only the electrode potential difference between the cathode and anode is important in fuel cells. The reversible cell potential can be obtained from the difference between the reversible electrode potentials at the cathode and anode.

$$E_{rev} = E^o - \frac{RT}{2F} \ln \left(\frac{a_{H_2O}}{a_{H_2} a_{O_2}^{1/2}} \right) \quad (2.10)$$

2.4 Electrode Kinetics

Electrochemical kinetics is a complex process and only a short summary is provided in this section. The first step in understanding the kinetics of the electrode is to determine the governing electrochemical reaction mechanism. The reaction mechanism can be single step or multi-step with electron transfer. The operation of an electrochemical system is a highly non-equilibrium process that involves the transfer of electrons and reactant species at the electrode surface. The reaction rates are directly related to the Faradic current flows through the electrode. This rate depends on three important parameters: exchange current density which is related to catalytic activity of the electrode surface, concentration of oxidizing and reducing species at the electrode surface, and surface activation overpotential. Mathematically, these physical quantities are used to derive the Butler-Volmer equation for calculating the current.

2.5 Over-potentials and Crossover Losses in Fuel Cells

The reversible potential obtained from the Nernst equation corresponds to the thermodynamic equilibrium state of the electrochemical system. However, when current starts flowing through the cell, the cell potential drops below the reversible potential due to several types of over-potential including activation over-potential, ohmic over-potential, and concentration over-potential. In addition to these typical electrochemical over-potentials, PEM fuel cells also suffer from other losses such as internal currents and fuel crossover even at open circuit. The details of these potential losses are described in the sections below.

2.5.1 Internal Currents and Fuel Crossover

Fuel crossover is the amount of fuel that crosses the membrane from the anode to the cathode without being oxidized at the anode catalyst layer, which results in a loss of fuel. Internal current is the flow of electron from the anode to the cathode through the membrane instead of going through the external circuit. The combination of these two losses is typically small compared to other types of losses.

2.5.2 Ohmic Over-potential

Two types of ohmic losses occur in fuel cells. These are potential losses due to electron transport through electrodes, bipolar plates, and collector plates; and potential loss due to proton transport through the membrane. The magnitudes of these potential losses depend on the materials used in the construction of the fuel cells and the operating conditions of the cell. Membrane conductivity increases with membrane water content.

2.5.3 Activation Over-potentials

The activation over-potential is the potential loss to drive the electrochemical reactions from equilibrium state. Therefore, it is the potential loss when there is a net current production from the electrode, i.e. a net reaction rate. In PEM fuel cell, the activation over-potential at the anode is negligible compared to that of the cathode. Activation polarization depends on factors such as the material property of the electrode material, ion-ion interactions, ion-solvent interactions and characteristics of the electric double layer at the electrode-electrolyte interface. Activation polarization may be reduced by increasing operating temperature and by increasing the active surface area of the catalyst.

2.5.4 Mass Transport Over-potential

Mass transport loss becomes significant when the fuel cell is operated at high current density. This is created by the concentration gradient due to the consumption of oxygen or fuel at the electrodes. The mass transport loss at the anode can be negligible compared to the cathode. At the limiting current density, oxygen at the catalyst layer is depleted and no more current can be increased from the fuel cell. This is responsible for the sharp decline in potential at high current densities. To reduce mass transport loss, the cathode is usually run at high pressure.

3 FUEL CELL MODEL

3.1 Computational Domain

To reduce computational demand and complexity, only one turn of the serpentine channel was used in the computational domain as shown in Figure 3.1.

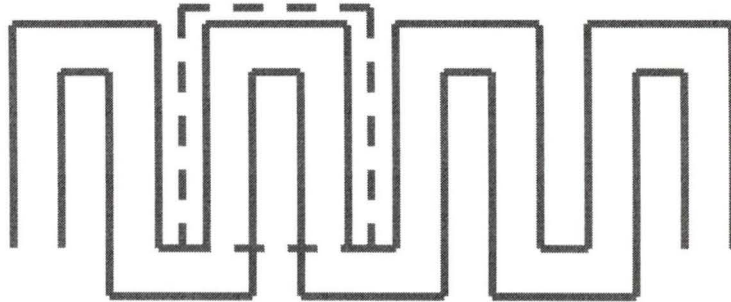


Figure 3.1. Selection of computational domain

The full computational domain consists of cathode and anode gas flow channels, membrane electrode assembly, bipolar plate as shown in Figure 3.2.

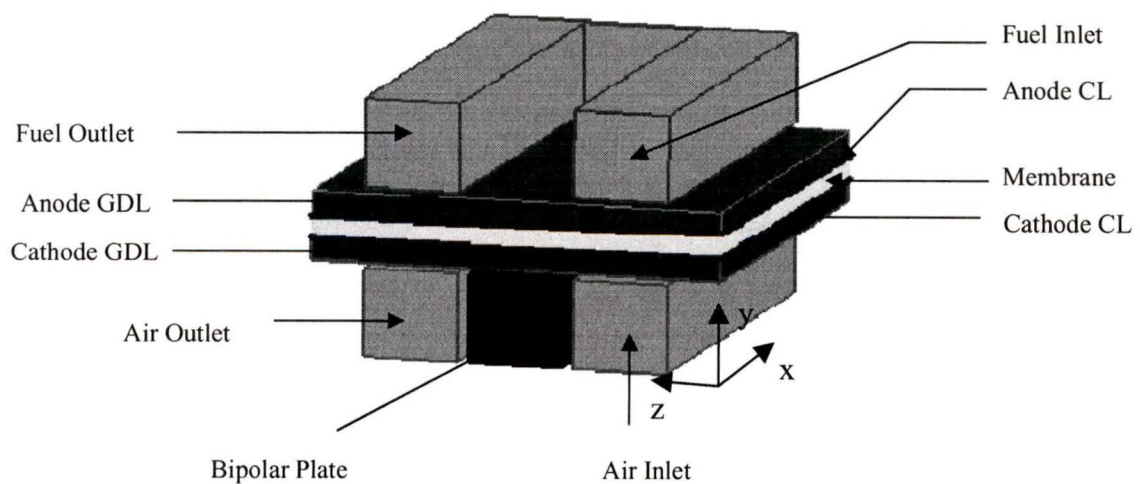


Figure 3.2. Computational domain

3.2 Modeling Equations

3.2.1 Flow in Gas Channels

Flow in gas channels are modeled as ideal gas flow in closed channels. The governing equations are:

Continuity equation:

$$\frac{\partial(\rho u)}{\partial x} + \frac{\partial(\rho v)}{\partial y} + \frac{\partial(\rho w)}{\partial z} = 0 \quad (3.1)$$

Momentum equation:

$$\begin{aligned} \frac{\partial(\rho uu)}{\partial x} + \frac{\partial(\rho uv)}{\partial y} + \frac{\partial(\rho uw)}{\partial z} &= -\frac{\partial P}{\partial x} + \frac{\partial}{\partial x} \left(\mu \frac{\partial u}{\partial x} \right) + \frac{\partial}{\partial y} \left(\mu \frac{\partial u}{\partial y} \right) + \frac{\partial}{\partial z} \left(\mu \frac{\partial u}{\partial z} \right) \\ \frac{\partial(\rho vu)}{\partial x} + \frac{\partial(\rho vv)}{\partial y} + \frac{\partial(\rho vw)}{\partial z} &= -\frac{\partial P}{\partial y} + \frac{\partial}{\partial x} \left(\mu \frac{\partial v}{\partial x} \right) + \frac{\partial}{\partial y} \left(\mu \frac{\partial v}{\partial y} \right) + \frac{\partial}{\partial z} \left(\mu \frac{\partial v}{\partial z} \right) \\ \frac{\partial(\rho wu)}{\partial x} + \frac{\partial(\rho wv)}{\partial y} + \frac{\partial(\rho ww)}{\partial z} &= -\frac{\partial P}{\partial z} + \frac{\partial}{\partial x} \left(\mu \frac{\partial w}{\partial x} \right) + \frac{\partial}{\partial y} \left(\mu \frac{\partial w}{\partial y} \right) + \frac{\partial}{\partial z} \left(\mu \frac{\partial w}{\partial z} \right) \end{aligned} \quad (3.2)$$

Energy equation:

$$\nabla \cdot (\rho \mathbf{u} H) - \nabla \cdot (k \nabla T) = 0 \quad (3.3)$$

H is the total enthalpy, given in terms of static (thermodynamic) enthalpy h by:

$$H = h + \frac{1}{2} \mathbf{u}^2 \quad (3.4)$$

ρ is the gas-phase density, $\mathbf{u}=(u,v,w)$ is the fluid velocity, P is pressure, T is temperature, μ is molecular viscosity, k is thermal conductivity.

These equations represent 5 transport equations in the 7 unknown u, v, w, P, T, ρ , and h .

The system of equation is closed by adding two more equations from thermodynamics.

First is the equation of state relating density to temperature and pressure

$$\rho_i = \frac{PM_i}{RT} \quad (3.5)$$

The gas mixture density, ρ , is calculated as follow,

$$\frac{1}{\rho} = \sum \frac{Y_i}{\rho_i} \quad (3.6)$$

The second is the constitutive equation relating static enthalpy to temperature and pressure,

$$h = \int_{T_{ref}}^T C_p dT \quad (3.7)$$

The mass transfer of each component is calculated as the mass fraction of a multi-component gas mixture that has the same form as the general convection-diffusion equation,

$$\nabla \cdot (\rho \mathbf{u} Y_i) - \nabla \cdot (\rho D \nabla Y_i) = 0 \quad (3.8)$$

Here the subscript i denotes oxygen or water vapor at the cathode side and hydrogen at the anode side. For the cathode side, the diffusion coefficient, D , is the diagonal element of the Stefan-Maxwell ternary diffusion coefficient matrix (Appendix A) for oxygen and water respectively; and for anode side, D is the binary diffusivity. The background fluid for the cathode side is nitrogen and for the anode side is water vapor respectively. Furthermore, the gas mixture is assumed well-mixed at the molecular level, and all

species share the same velocity, pressure and temperature fields in their immediate environment.

The molar fraction, x_i , of each species is calculated from the mass fraction based on a relation given by Bird et al. [6],

$$x_i = \frac{\frac{Y_i}{M_i}}{\sum_{j=1}^n \frac{y_j}{M_j}} \quad (3.9)$$

3.2.2 Gas Diffusion Layers

Transport in the gas diffusion layers (GDL) is modeled as transport in porous media. The volume porosity ε is defined as the ratio of the volume V' available for flow and the physical volume V of the cell. Therefore,

$$V' = \varepsilon V \quad (3.10)$$

The continuity equation in the gas diffusion layers becomes,

$$\nabla \cdot (\rho \varepsilon \mathbf{u}) = 0 \quad (3.11)$$

The momentum equation reduces to Darcy's law,

$$\mathbf{u} = -\frac{k_p}{\mu} \nabla P \quad (3.12)$$

The mass transport equation in the GDL becomes,

$$\nabla \cdot (\rho \varepsilon \mathbf{u} Y_i) - \nabla \cdot (\rho \varepsilon D \nabla Y_i) = 0 \quad (3.13)$$

The diffusivities are corrected for the flow in porous media by using the Bruggemann correction formula,

$$D_{ij}^{eff} = D_{ij} * \varepsilon^{1.5} \quad (3.14)$$

Heat transfer in the in the gas diffusion layers can be modeled by,

$$\nabla \cdot (\rho \varepsilon \mathbf{u} H) - \nabla \cdot (\lambda_{eff} \varepsilon \nabla T) = \varepsilon Q \quad (3.15)$$

Where λ_{eff} is the effective thermal conductivity and Q contains the heat source or sink to or from the porous medium.

The effective thermal conductivity λ_{eff} can be calculated from the thermal conductivities of gas and graphite by an expression given by Gurau et al. [19],

$$\lambda_{eff} = -2\lambda_{gr} + \frac{1}{\frac{\varepsilon}{2\lambda_{gr} + \lambda_g} + \frac{1-\varepsilon}{3\lambda_{gr}}} \quad (3.16)$$

However, the effective thermal conductivity of Ballard Arvcarb[®] was used in this model.

3.2.3 Catalyst Layers

The catalyst layers are the most important regions of the computational domain. This is where electrochemical reactions are taking place which consume or generate the species available in the fuel cell. More specifically, sink and source terms are used to model the consumption or production of these species as follow (electrochemical kinetics is dealt with in a subsequent section).

At the cathode catalyst layer, oxygen consumption is modeled as a sink term based on the cathode local current density,

$$S_{O_2} = -\frac{M_{O_2}}{4F} i_c \quad (3.17)$$

The production of water is modeled as a source term based on the local current density,

$$S_{H_2O} = \frac{M_{H_2O}}{2F} i_c \quad (3.18)$$

At the anode catalyst layer, hydrogen is consumed to produce electrons and protons. The consumption of hydrogen is modeled as a sink term similar to that of oxygen consumption.

$$S_{H_2} = -\frac{M_{H_2}}{2F} i_a \quad (3.19)$$

Heat generation is due to the ohmic losses in the cathode and anode GDLs, potential loss due to resistance to proton transport in the membrane, and electrochemical reactions. However, only heat generation from the cathode reaction is considered in this model. Since the activation overpotential in the anode side is very small, heat generation at the anode side is negligible compared to the heat generation at the cathode side. Heat generation due to electrochemical reaction at the cathode side is given by Lampinen et al. [26],

$$\dot{q} = \left[\frac{T(-\Delta s)}{n_e F} + \eta_{act,c} \right] i_c \quad (3.20)$$

Where T is the local temperature, Δs is the entropy of the chemical reaction, n_e is the number of electrons transferred in one reaction, and $\eta_{act,c}$ is the cathode activation overpotential.

3.2.4 Membrane

The membrane is assumed fully humidified. The net water flux is modeled as the electro-osmotic drag of water from anode to cathode and back diffusion from cathode to anode

$$N_w = n_d M_w \frac{i}{F} - \nabla \cdot (\rho D_w Y_w) \quad (3.21)$$

Where n_d is the electro-osmotic drag coefficient and D_w is the water diffusion coefficient in the membrane.

3.2.5 Bipolar Plates

The bipolar plate conducts heat and electrons. Electron conduction is very fast in the graphite bipolar plate and the potential loss due to electron transport in the bipolar plate is assumed negligible. Therefore, the bipolar plate is modeled as a heat-conducting solid only,

$$\nabla \cdot (\lambda_{gr} \nabla T) = 0 \quad (3.22)$$

3.3 Potential Drop Across the Cell

The goal in this section is to model the potential losses in the gas diffusion layers and membrane, so that the activation overpotential can be accurately predicted

3.3.1 Ohmic Loss in Gas Diffusion Layers

The potential loss due to current conduction through the gas diffusion layer can be modeled by an equation similar to the Laplace equation. The potential boundaries are setup to drive the current through these regions,

$$\nabla \cdot (\lambda_e \nabla V) = S_e \quad (3.23)$$

Where S_e is the electron source term equals to the anode and cathode currents for each side respectively. The ohmic loss is then calculated as,

$$\eta_{ohmic} = V_{CL} - V_{ref} \quad (3.24)$$

Where V_{CL} is the potential at the catalyst layer and V_{ref} is the reference potential set at the interface between the gas diffusion layer and the bipolar plate.

3.3.2 Ohmic Loss in Membrane

Potential loss in the membrane is due to resistance to proton transport across the membrane. This potential loss distribution is also modeled by the Laplace equation similar to the potential loss in the gas diffusion layer regions,

$$\nabla \cdot (\lambda_m \nabla V) = S_m \quad (3.25)$$

Where S_m is source and sink of protons in the anode catalyst layer and cathode catalyst layer respectively. The protonic loss is then calculated as,

$$\eta_{protonic} = V_{CL,c} - V_{CL,a} \quad (3.26)$$

Where $V_{CL,c}$ is the potential at the cathode catalyst layer and $V_{CL,a}$ is the potential at the anode catalyst layer.

3.3.3 Activation Over-potential

After the ohmic losses in the membrane and gas diffusion electrodes are calculated, activation over-potential can be calculated from the reversible potential and cell potential,

$$\eta_{act,c} = E_{rev} - E_{cell} - \eta_{ohmic,gdl} - \eta_{protonic,mem} \quad (3.27)$$

The cell reversible potential, E_{rev} , is a thermodynamic property and can be calculated based on Nernst equation as described in Section 2.3. The cell potential, E_{cell} , is the input parameter based on the desired loading condition. Therefore the cathode activation

overpotential can be determined. The anode activation overpotential is small and considered negligible in this model.

3.4 Electrochemical Kinetics

The local current density is calculated based on the well known Butler-Volmer equation which couples the reactant concentration with the activation overpotential:

Cathode current,

$$i_c = i_{o,c}^{ref} \left(\frac{C_{O_2}}{C_{O_2}^{ref}} \right)^{\gamma_{O_2}} \left[\exp\left(\frac{\alpha_a F}{RT} \eta_{act,c} \right) - \exp\left(-\frac{\alpha_c F}{RT} \eta_{act,c} \right) \right] \quad (3.28)$$

where $i_{o,c}^{ref}$ is the cathode reference exchange current density, α_a and α_c are the cathode anodic and cathodic charge transfer coefficients respectively.

Anode current,

$$i_a = i_{o,a}^{ref} \left(\frac{C_{H_2}}{C_{H_2}^{ref}} \right)^{\gamma_{H_2}} \left[\exp\left(\frac{\alpha_a F}{RT} \eta_{act,a} \right) - \exp\left(-\frac{\alpha_c F}{RT} \eta_{act,a} \right) \right] \quad (3.29)$$

However, the anode current is simplified in this model. Since the anode activation overpotential is very small and the hydrogen concentration distribution at the catalyst layer is quite uniform, the local anode current density is set equal to the average cathode current density with the condition that charge must be conserved,

$$I_{total} = \sum_{j=1}^{N_c} i_{c,j} \times V_j = \sum_{j=1}^{N_a} i_{a,j} \times V_j \quad (3.30)$$

Where N_c and N_a are the total number of cells in the cathode and anode catalyst layers respectively; V_j is the cell volume.

3.5 Boundary Conditions

Boundary conditions are specified at all external boundaries of the computational domain as well as boundaries for various mass transport and scalar equations inside the computational domain.

3.5.1 Inlets

At the anode and cathode several Dirichlet boundary conditions of velocity, inlet gas stream temperature, mass fraction of each gas component are applied as follows: the inlet velocity is a function of the cell current and stoichiometric flow ratio, MEA area, and channel cross-section area. In other words, the inlet mass flow must be sufficient to supply the amount of reacting species required for a specific current density and stoichiometric flow ratio. In this model, the cell current is predicted from a specified cell voltage, therefore cell current is changing at every iteration, and hence the inlet velocity must be updated at every iteration to keep up with the changing cell current.

The inlet velocity is calculated as,

$$U_{inlet} = \frac{\xi I}{n_e F} \frac{A_{MEA}}{A_{Ch}} \frac{RT}{x_i P_i} \quad (3.31)$$

Where n_e is the number of electrons per mole of reactant species, $n_e = 4$ for oxygen at the cathode and $n_e = 2$ for hydrogen at the anode, ξ is the stoichiometric flow ratio. P_i is the total gas pressure and x_i is the molar fraction of hydrogen or oxygen at the anode or cathode respectively.

3.5.2 Outlets

Pressure boundary conditions are specified at the anode and cathode outlets. The desired cell operating pressures are specified at the anode and cathode outlets. Neumann boundary conditions are applied for other variables, i.e. zero normal gradients are imposed on velocity, temperature, species mass fractions, and the additional scalar equations of the potential fields. Mathematically, this is stated as,

$$\frac{\partial \phi}{\partial x} = 0 \quad (3.32)$$

where ϕ is any variable (except pressure).

3.5.3 External Surfaces

Symmetry boundary conditions are applied at the surfaces of the computational domain in the z-direction. All variables are mathematically symmetric, with no flux across the boundary. At the external surfaces in the y-direction, (top and bottom surfaces of the cell), temperature is specified and zero heat flux is specified,

$$\frac{\partial T}{\partial y} = 0 \quad (3.33)$$

3.5.4 Boundary Conditions at the Interfaces inside the Computational Domain

At the boundary between the gas channel and the bipolar plate, conducting boundary condition is applied to account for heat transfer between these two materials. Perhaps the most difficult boundary conditions to apply are the boundary conditions required for the

mass fraction equations and the potential equations at the interfaces between different regions of the cell.

For the oxygen mass fraction equation, a boundary condition must be specified at the interface between the cathode catalyst layer and the membrane to keep the oxygen from entering the membrane. A Neumann type boundary condition was specified here,

$$\frac{\partial Y_{O_2}}{\partial y} = 0 \quad (3.34)$$

Similarly, a Neumann type boundary condition was applied at the interface between the anode catalyst layer and the membrane to stop hydrogen from entering the membrane. This boundary can be mathematically stated by,

$$\frac{\partial Y_{H_2}}{\partial y} = 0 \quad (3.35)$$

The potential equations also required a combination of Dirichlet and Neumann boundary conditions at the interfaces in the y direction. Dirichlet boundary conditions are applied at the interface between the bipolar plates and the gas diffusion layers. More specifically, a zero potential boundary is specified at this interface. Neumann boundary conditions are applied at the interface between the gas channels and the gas diffusion layers to give zero potential flux into the gas channels. Mathematically at these interfaces the potential gradient is zero,

$$\frac{\partial V}{\partial y} = 0 \quad (3.36)$$

Similarly, the protonic potential field requires a set of potential boundary condition and zero flux boundary condition at the anode catalyst layer interface and cathode catalyst layer interface respectively.

3.6 Computational Procedure and Solution Algorithm

A commercial computational fluid dynamics (CFD) code, CFX-4.4, was used as the backbone for the implementation of the model. The codes solves for the standard thermo-fluid transport equations, and user defined subroutines were developed for the parts of the model specific to fuel cell physics. All transport equations are discretized based on the finite volume method into a system of algebraic equations which can be solved by an iterative algorithm. The computational domains are divided into a finite number of control volumes (cells). All variables are stored at the centroid of each cell. The iteration process is divided into two levels: an inner iteration to solve for the spatial coupling for each variable and an outer iteration to solve for the coupling between the variables. Thus each variable is taken in sequence, regarding all other variables as fixed, a discrete transport equation for that variable is formed for every cell in the flow domain and the problem is passed over to a linear equation solver, which returns the updated values of the variable. The pressure is solved based on the SIMPLEC algorithm.

3.6.1 Inner Iteration

The set of linearised difference equations for a particular variable, one equation for each control volume in the flow, is passed to a simultaneous linear equation solver which uses

an iterative solution method. An exact solution is not required because this is just one step in the non-linear outer iteration. The equation solver chosen for each variable is listed in Table 3.1. Controlling the inner iteration is important in achieving convergence of the solution process. The computational effort which may be expended in obtaining a reasonable solution to the set of equations must now be specified. These parameters which control the solution process are minimum number of iteration (MNSL), maximum number of iteration (MXSL), and residual reduction factor (RDFC).

Variable	Finite Difference Scheme	Equation Solver
U	QUICK	Full field Stone's Method
V	QUICK	Full field Stone's Method
W	QUICK	Full field Stone's Method
P	CDS	Full field Stone's Method
T	QUICK	Full field Stone's Method
H	QUICK	Full field Stone's Method
Mass Fractions	QUICK	Full field Stone's Method
Scalar Equations	QUICK	Full field Stone's Method

Table 3.1 Difference scheme and linear equation solver used for each variable.

3.6.2 Outer Iteration

The outer iteration loop can be used to control the convergence of the solution process. A maximum number of global iterations is set. Other convergence criteria such as residual

values are also set at the outer iteration to monitor the solution. At the end of each outer iteration, the values of the residuals are printed for each of the active variables and plotted on the dynamic plot utility for convergence monitor. In addition to the residual values, values of oxygen mass fraction, current density, and activation over-potential are also plotted dynamically with the solution process.

3.6.3 Solution Algorithm

As pointed out earlier, multi-dimensional models presented to date assume constant activation overpotential in order to simplify the numerical procedure and allow for the calculation of the activation overpotential a posteriori. The algorithm developed in this model is unique in the way of predicting cell current density from a specific input cell operating voltage. The solution begins by guessing a current to use for calculating the inlet flow rates at the anode and cathode sides. Then follows by computing the flow fields for velocities u, v, w , and pressure p . Once the flow field is obtained, the mass fraction equations are solved for the mass fractions of oxygen, hydrogen, water vapor, and nitrogen. Scalar equations are solved last in the sequence of the transport equations for the temperature field in the cell and potential fields in the gas diffusion layers and the membrane. After the potential equations are solved, the activation over-potential can be readily obtained from equation (3.27). The local current densities are solved based on the Butler-Volmer equation (3.28). Convergence criteria are then performed on each variable and the procedure is repeated until convergence. The flowchart diagram of the algorithm is shown in Figure 3.3.

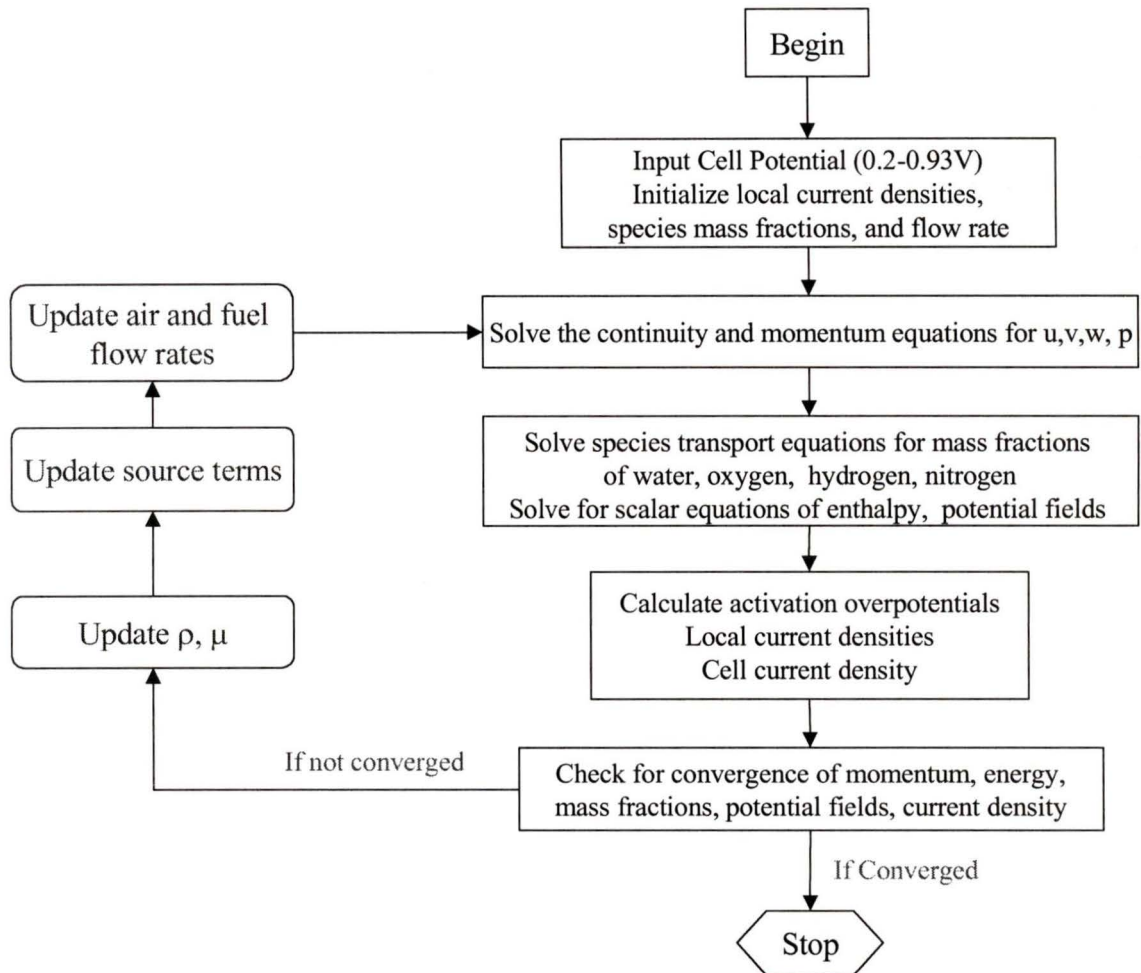


Figure 3.3. Voltage-To-Current (VTC) algorithm.

3.7 Modeling Parameters

Choosing the right modeling parameters is important in establishing the base case validation for the model against experimental results. Very limited experimental results are available in the literature with detailed specifications of the cell geometry and experimental conditions. However, courtesy of Professor Hongtan Liu, raw experimental results used to verify his 3-D model in [40] were made available to us. The dimensions of the computational domain used in this thesis are listed in Table 3.2

Parameter	Symbol	Value	Unit
Channel Length	L	50	mm
Channel Height	H	1	mm
Channel Width	W_c	1	mm
Channel divider height		1	mm
Channel divider Width		1	mm
Electrode thickness	t_e	0.26	mm
Catalyst layer thickness	t_{cl}	0.0287	mm
Membrane thickness	t_{mem}	0.23	mm

Table 3.2 Cell dimensions for base case.

The operational parameters are based on the experimental operating conditions used by Wang et al. [40]. These values are listed in Table 3.3. Operating parameters have a

large impact on fuel cell performance and these will be examined in the parametric study section.

Parameter	Symbol	Value	Unit
Air pressure	P_c	3	atm
Fuel pressure	P_a	3	atm
Air stoichiometric flow ratio	ξ_c	3	-
Fuel stoichiometric flow ratio	ξ_a	3	-
Relative humidity of inlet fuel	φ_a	100%	-
Relative humidity of inlet air	φ_c	100%	-
Air inlet temperature	T	353	K
Fuel inlet temperature	T	353	K

Table 3.3 Operating conditions for base case.

Electrode material properties have important impact on fuel cell performance. The important electrode material properties are thickness, porosity, and thermal and electronic conductivities. Electrode thickness and porosity can affect the mass transport of all reactant and product species and the ohmic overpotential due to current conduction in the electrode. The base case values are listed in Table 3.4.

Parameter	Symbol	Value	Ref.
Electrode porosity	ϵ	0.4	[3]
Electrode hydraulic permeability	k_p	4.73E-19 m ²	[3]
Electrode thermal conductivity (Ballard AvCarb [®] -P150)	λ_{eff}	1.3 W/mK	-
Electrode electronic conductivity (Estimate)	λ_e	570 S/m	-
Anodic charge transfer coefficient for cathode reaction	$\alpha_{a,c}$	2	-
Cathodic charge transfer coefficient for the cathode reaction	$\alpha_{c,c}$	2	-
Anode reference exchange current density	$ai_{o,c}^{\text{ref}}$	1.4E5 A/cm ³	[3]
Cathode exchange current density	$ai_{o,a}^{\text{ref}}$	1.0E-5 A/cm ³	[3]
Oxygen concentration parameter	γ_{O_2}	0.5	[3]
Hydrogen concentration parameter	γ_{H_2}	0.25	[3]

Table 3.4 Electrode properties at base case conditions

The membrane properties are required to model various transport phenomena across the membrane. Properties required in this model are electro-osmotic drag coefficient, membrane electronic conductivity, and diffusion coefficients for water back diffusion. All of these parameters are taken based on a fully humidified membrane; and are listed in Table 3.5.

Parameter	Symbol	Value	Ref.
Protonic diffusion coefficient	\mathcal{D}_{H^+}	4.5E-9 m ² /s	[3]
Fixed charge concentration	c_f	1200 mol/m ³	[3]
Fixed-site charge	z_f	-1	[3]
Electrokinetic permeability	K_Φ	7.18E-20 m ²	[3]
Hydraulic permeability	k_p	1.8E-18 m ²	[3]
Effective Thermal conductivity	λ_{eff}	0.455 W/mK	[23]
Protonic conductivity	κ	0.17 S/cm	[3]
Electro-osmotic drag coefficient		2.5	[37]

Table 3.5. Membrane properties

The binary gas diffusion coefficients were taken from [10] and are shown in Table 3.6.

The binary diffusivities of the gases are also dependent on temperature and pressure based on a relation given by Cussler [10],

$$D_{ij}^{eff}(T, P) = D_{ij}(T_o, P_o) \frac{P_o}{P} \left(\frac{T}{T_o} \right)^{1.75} \quad (3.37)$$

Gas Pair	T_0 (K)	D_{ij} (cm ² /s)
H ₂ -H ₂ O	307.1	0.915
O ₂ -H ₂ O	308.1	0.282
O ₂ -N ₂	293.2	0.220
H ₂ O-N ₂	307.5	0.256

Table 3.6 Binary diffusivities at 1 atm.

4 MODEL VALIDATION AND RESULTS

4.1 Model Validation

4.1.1 Comparing with Experimental Data

The results for base case operating conditions were verified with experimental results provided by Wang et al. [40]. The polarization curve of cell potential versus cell current density for the model is in good agreement with the experimental polarization curve in the low and intermediate load regions. However, the model cell current densities in the mass transport limitation region ($> 1.25 \text{ A/cm}^2$) are higher than the experimental values. This over prediction of cell current is due to the one phase nature of the model, i.e. the effect of reduced oxygen transport due to water flooding at the cathode at high current density is not accounted for. In addition to the cathode flooding effect, the anode drying is also a contributing factor to the reduced performance at high current density.

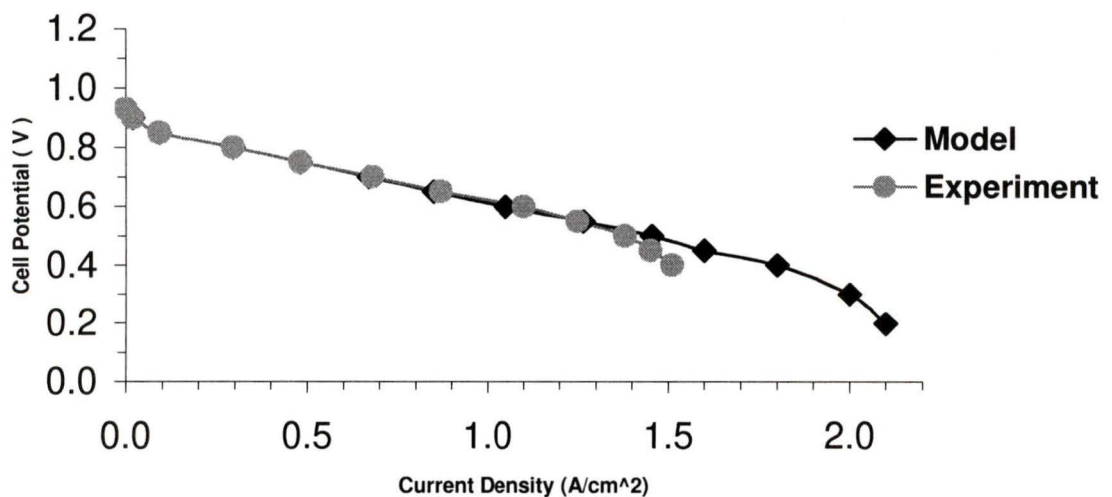


Figure 4.1. Comparison of model and experimental polarization curves.

Similar to the polarization curve, the model power density curve shows good agreement with the experimental curve in the load region below the mass transport region. At high load condition, the predicted values are higher than the experimental values as expected. At this point, it should be noted that at present time, the polarization curve is the only experimental data that are available in the literature, therefore polarization curves are commonly used to validate the agreement between model and experiments. However, the polarization curve agreement can also be achieved with 1-D models that have been published. Therefore, strict validation would require detailed data comparison from local distributions of current densities, species concentrations etc.... Such data are very difficult to obtain and are not currently available in the literature.

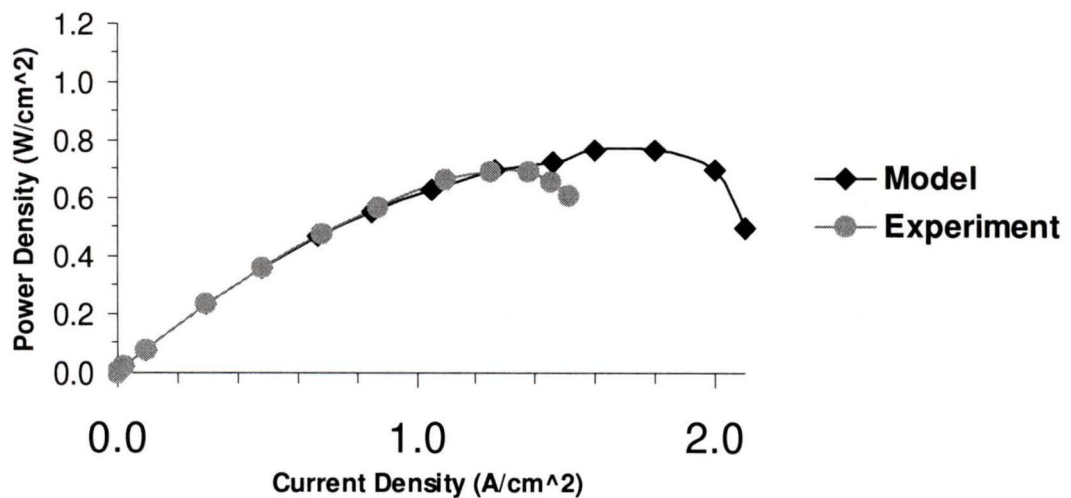


Figure 4.2. Comparison of model and experimental power density curves

4.1.2 Grid Study

The convergence behavior and accuracy of a numerical solution depends on the discretization scheme, equation solver algorithm, and grid quality. In general, a finer grid provides more accurate solution. However, larger grid size will increase the computational power required to carry out the simulation. Therefore, it is important to find the grid size that is just adequate to provide the accuracy needed for the simulation. In this study, a grid of 20% finer than the base case grid was used for comparison. The base case mesh has 351000 cells and the refined mesh has 421200 cells. The polarization curves (Figure 4.3) for the two cases show that there is no significant difference between the two results. Therefore, the base case mesh is sufficient and no further refinement is necessary, considering the increase in computational cost for finer mesh.

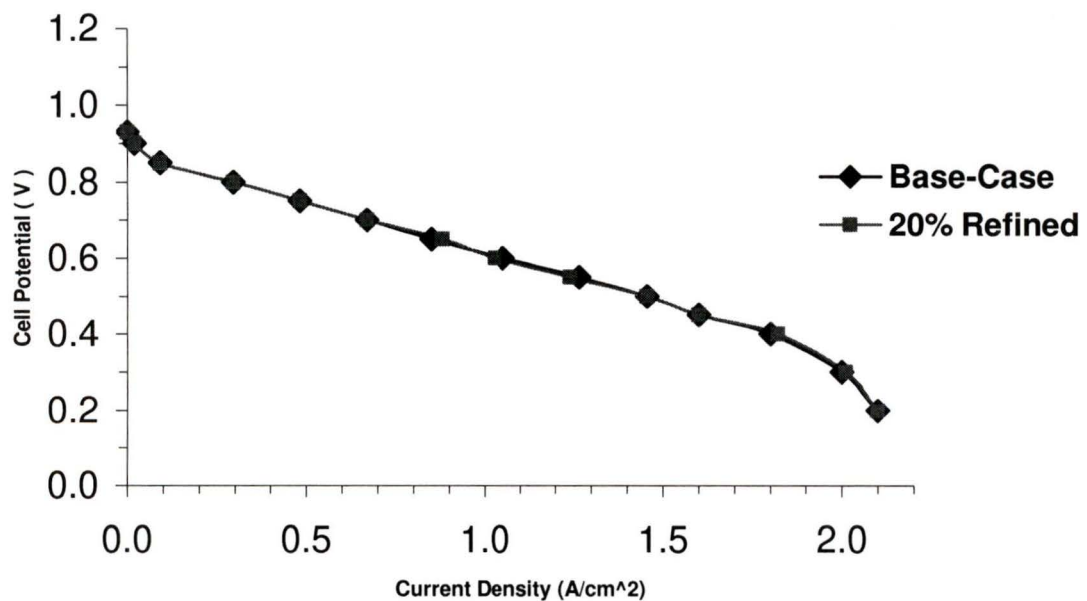


Figure 4.3. Polarization curves comparing base case mesh and refined mesh results.

4.2 Base Case Results and Discussions

In addition to the polarization and power curves, the comprehensive three-dimensional model also allows for the assessment of important information about the detail of transport phenomena inside the fuel cell. These transport phenomena are the distribution of local reactant gas concentrations, temperature field, local current densities, potential fields, and activation overpotentials.

4.2.1 Velocity Profile

The velocity profile in the serpentine channel turn has a few distinctive characteristics. Far away from the turning region, the velocity exhibits a laminar fully developed profile where the highest velocity is located at the center of the channel. However, as the flow approaches the turning region, separation occurs and the symmetric velocity profile becomes asymmetric with the highest velocity closer to the inner wall. Three recirculation zones are observed: two at the top corners and one at the channel divider. As the flow leaves the turning region, the asymmetric velocity profile remains. Further downstream from the turning region, the symmetric velocity profile becomes fully developed again and this profile is maintained until the end of the channel.

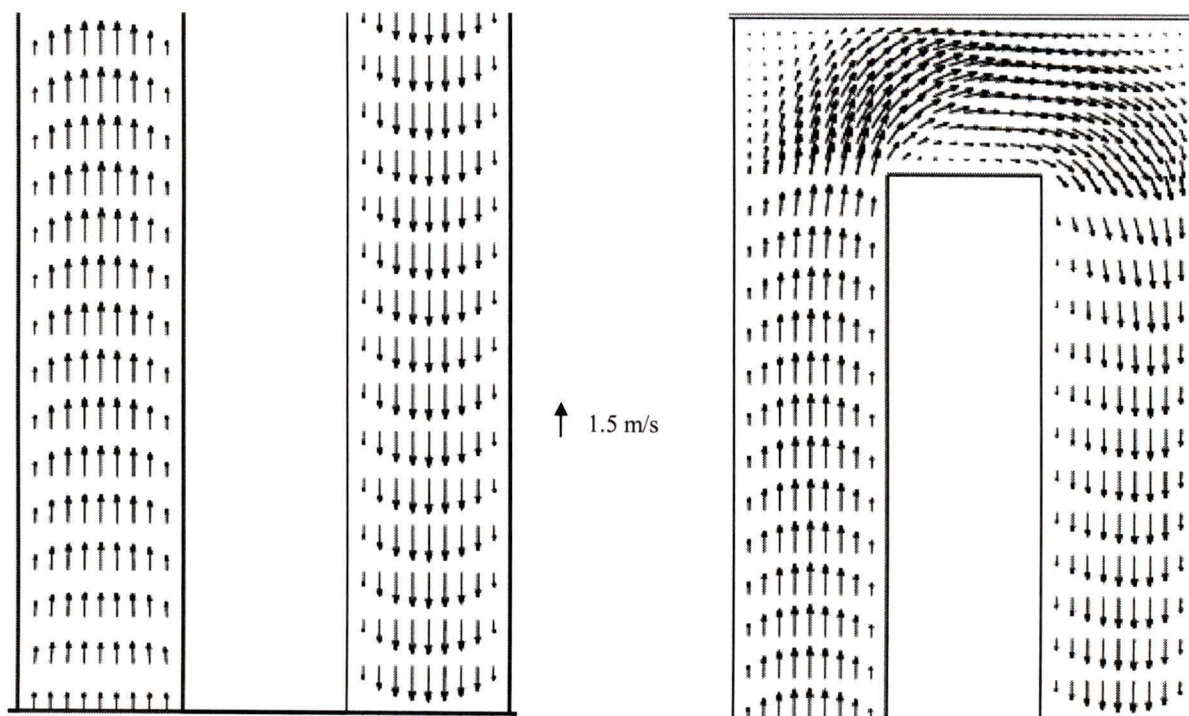


Figure 4.4. Velocity profile of the turning, inlet, and outlet regions in the cathode gas channel with a load of 1.2 A/cm^2 and $\text{Re} = 71.7$.

4.2.2 Oxygen Distribution

The transport limitation of oxygen has a large effect on the performance of PEM fuel cell. Therefore, it is important to understand the behavior of oxygen transport in the cathode channel, GDL, and catalyst layer. Figure 4.5 shows the oxygen distribution in the cathode side under three different loading conditions. In all cases, oxygen concentration decreases gradually from inlet to outlet due to the consumption of oxygen at the catalyst layer. Another common feature is the distribution in the GDL, where oxygen

concentration is higher under the channel area than under the land area. As the loading condition increases, the mass transport limitation of oxygen under the land area becomes significant. For the load of 1.2 A/cm^2 , oxygen under the land area is almost depleted.

4.2.3 Hydrogen Distribution

The hydrogen molar fraction distribution in the anode channel and gas diffusion layer is shown in Figure 4.6 for three different loading conditions. In general, the hydrogen concentration decreases from inlet to outlet as it is being consumed. However the decrease is quite small along the channel due to high diffusivity. Also, there is increase in hydrogen mass transport in the turning region for low load conditions of 0.3 and 0.69 A/cm^2 .

4.2.4 Activation Overpotential Distribution in the Cathode Catalyst Layer

Figure 4.7 shows the cathode activation overpotential distribution in the first sub-layer (GDL/catalyst layer interface) of the catalyst layer. In all loading conditions, the distribution patterns of activation overpotentials are similar, with higher activation overpotentials under the land area. This uneven distribution is mainly due to the lower ohmic loss under the land area than under the channel area. Since activation overpotential has an exponential effect on the magnitude of local current, it can be deduced that the potential condition for producing current under the land area is more favorable in the absence of oxygen transport limitation. This argument is supported by the current density distribution pattern shown on Figure 4.8.

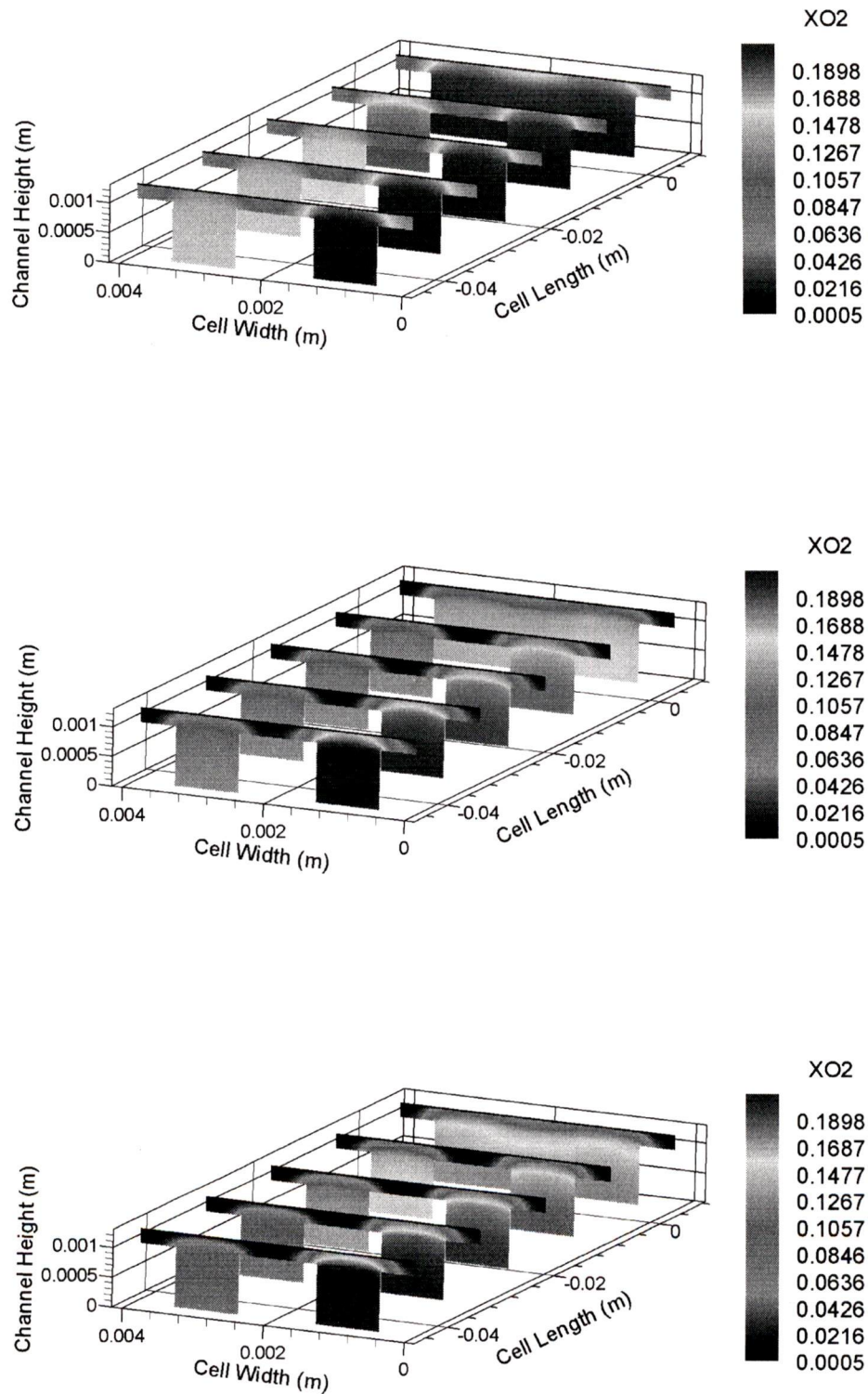


Figure 4.5. Oxygen molar fraction distribution in the cathode side for three loading conditions: 0.3 A/cm^2 (top), 0.69 A/cm^2 (middle), and 1.2 A/cm^2 (bottom).

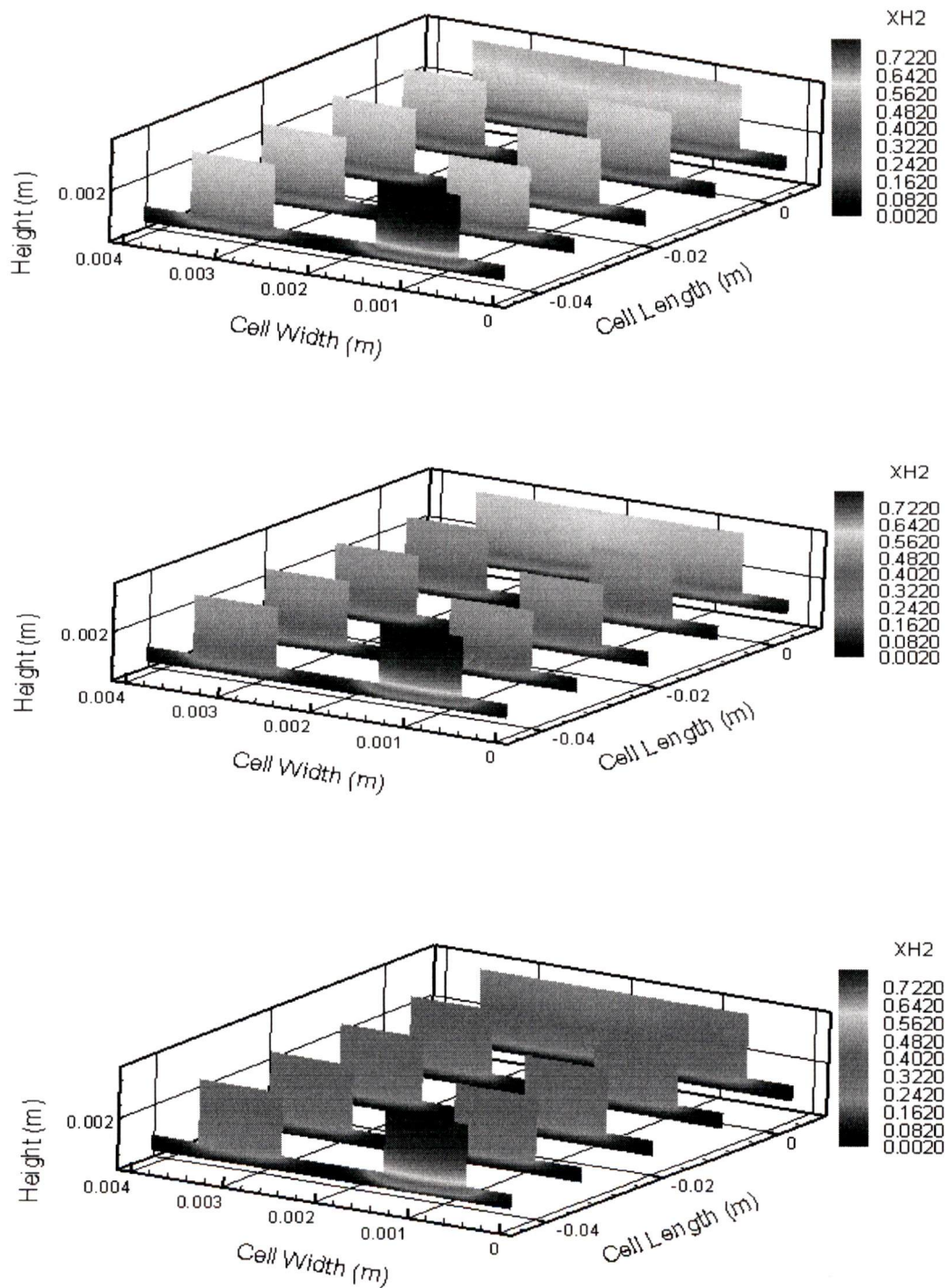


Figure 4.6. Hydrogen molar fraction distribution in the anode side for three loading conditions: 0.3 A/cm² (top), 0.69 A/cm² (middle), and 1.2 A/cm² (bottom).

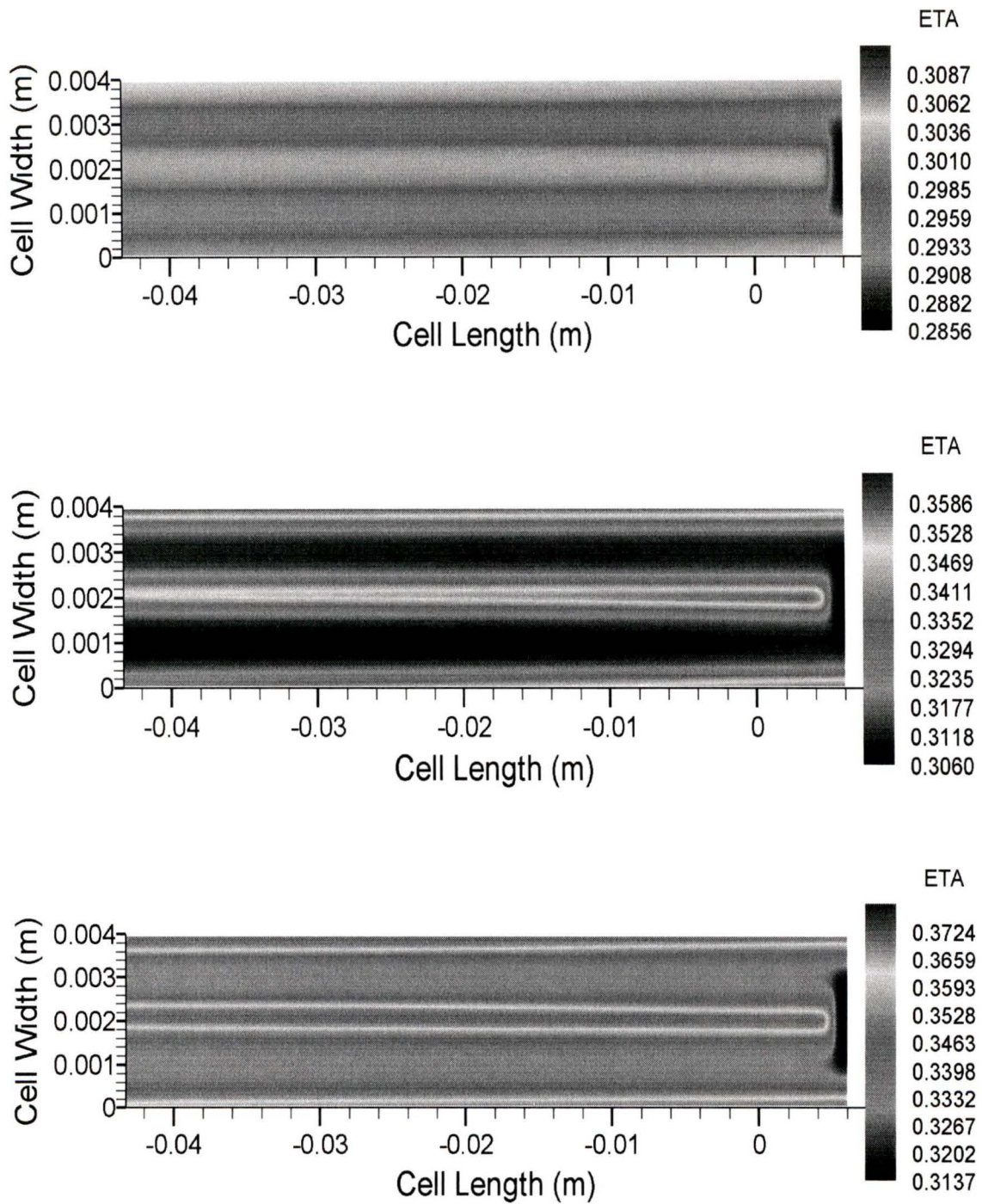


Figure 4.7. Activation overpotential distribution in the first catalyst layer for three loading conditions: 0.3 A/cm² (top), 0.69 A/cm² (middle), and 1.2 A/cm² (bottom).

4.2.5 Current Density Distribution

Since local current density is a function of oxygen concentration and activation overpotential, it is expected that the distribution patterns of oxygen concentration and activation overpotential have a major impact on the current density distribution under different loading conditions. Figure 4.8 shows the current density distribution for three loading conditions. For low load condition, the effect of oxygen transport is small, i.e. the concentration of oxygen under the land area is still high, therefore the current density is higher under the land area since the activation overpotential is higher under the land area as mentioned before. However, as the loading condition increases, the oxygen transport limitation under the land area become significant which results in the shift of current maxima towards the center of the channel where oxygen concentration is highest. The variation along the channel is not as large as the variation between the channel and land area. The current density generally decreases from inlet to outlet as the oxygen concentration decreases. Also for high load condition, the current at the outlet is almost entirely located under the channel area.

The variation of current density along the catalyst layer thickness is shown in Figure 4.9. Where the top sub-layer is adjacent to the membrane and the bottom sub-layer is adjacent to the GDL. This figure shows that most of the activity occurs on the bottom layer. This means that most of the oxygen is depleted in the first catalyst layer. However, under small load condition, there is also some small activity in the upper layers.

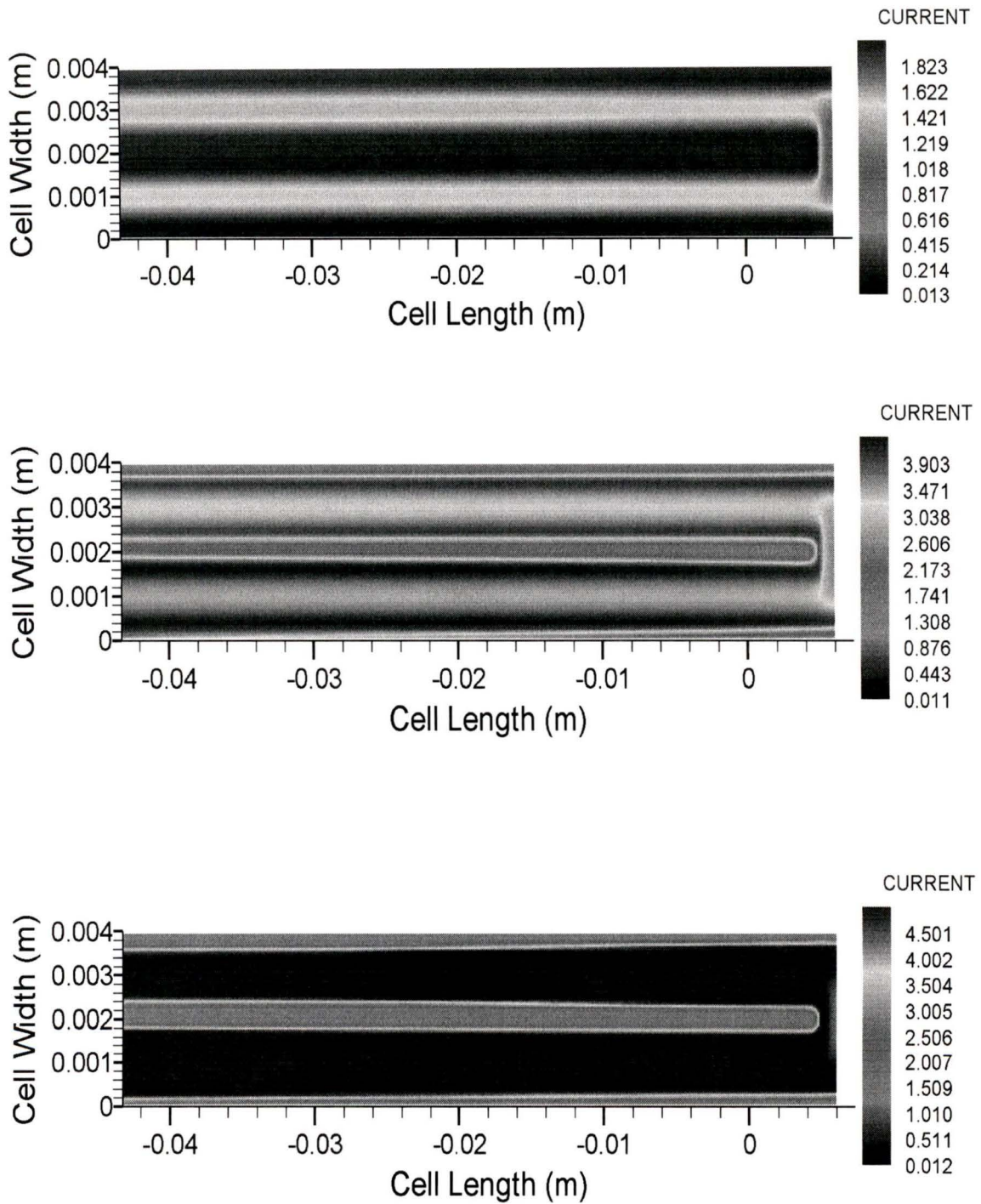


Figure 4.8. Relative current density distribution for three loading conditions: 0.3 A/cm² (top), 0.69 A/cm² (middle), and 1.2 A/cm² (bottom).

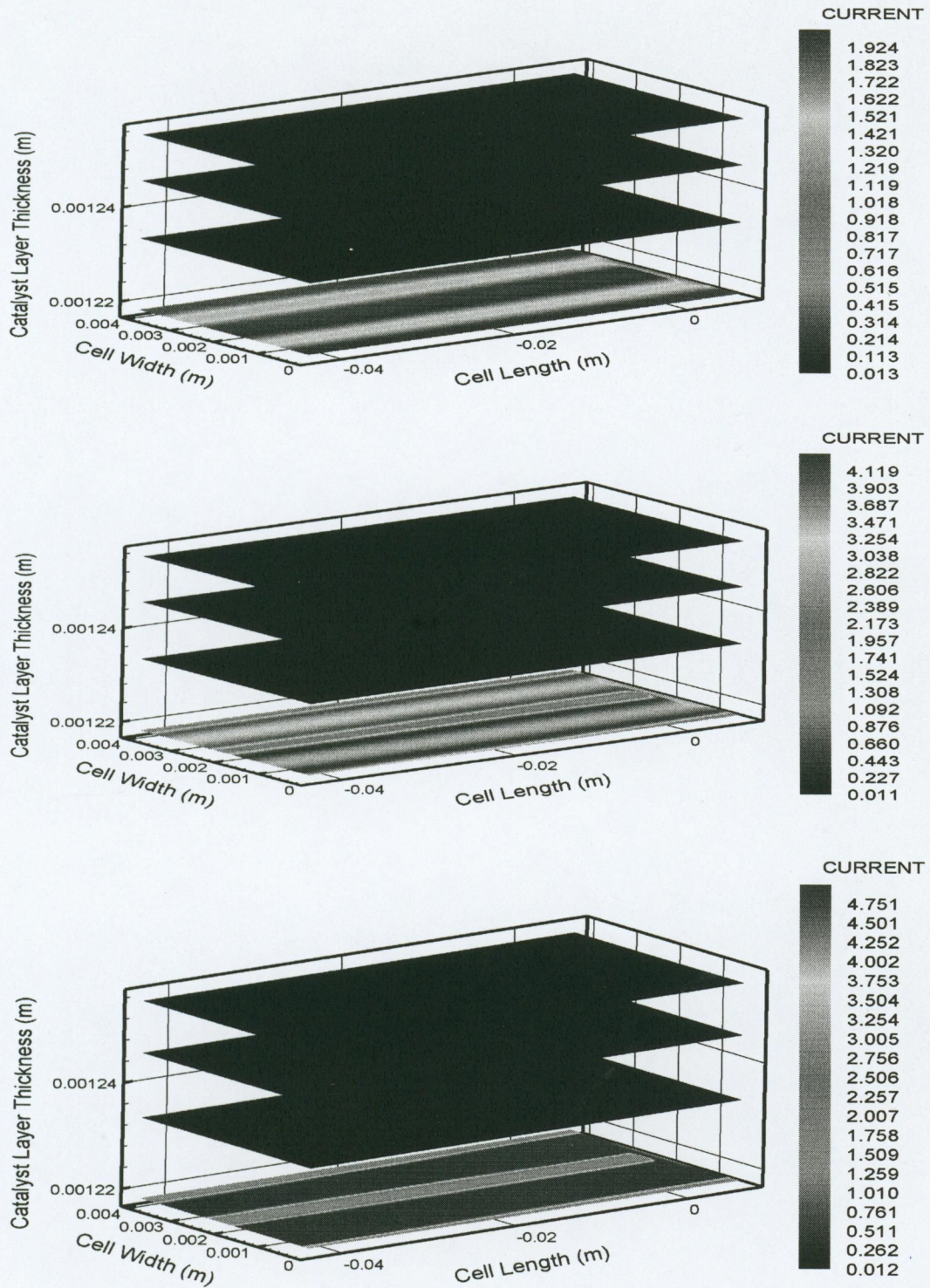


Figure 4.9. 3-D view of current density distribution in the cathode catalyst layer for three loading conditions: 0.3 A/cm² (top), 0.69 A/cm² (middle), and 1.2 A/cm² (bottom).

4.2.6 Ohmic Overpotential

Ohmic overpotential is the voltage loss due to resistance to electron transport in the gas diffusion layers. For a given load, the magnitude of this overpotential is dependent on the path traveled by the electrons. The longer the path, the larger the potential drop. Therefore the ohmic loss under the channel area is higher than the loss under the gas diffusion layer since the electrons have to travel a longer distance to reach the catalyst layer under the channel area. Figure 4.10 shows that the ohmic overpotential distribution patterns are similar for all three loading conditions. However, the magnitude of the potential loss increases with cell loading.

4.2.7 Membrane Overpotential

The potential loss in the membrane is due to resistance to proton transport across the membrane from anode catalyst layer to cathode catalyst layer. The distribution pattern of the protonic overpotential is also dependent on the path traveled by the protons and the activities in the catalyst layers. Figure 4.11 shows the potential loss distribution in the membrane for three loading cases. At low loading condition, the potential drop under the land area is higher because the catalytic activity is higher. However, at high load condition the potential drop is more uniformly distributed across the membrane. It is expected that at high load, more protons are produced under the channel area at the anode catalyst layer because the activity is quite high such that the hydrogen concentration under the land area would be low. Combining this effect with the current density distribution in the cathode catalyst layer where protons are consumed and where the activity is higher under the channel area, results in the more uniform overpotential distribution observed for high load condition.

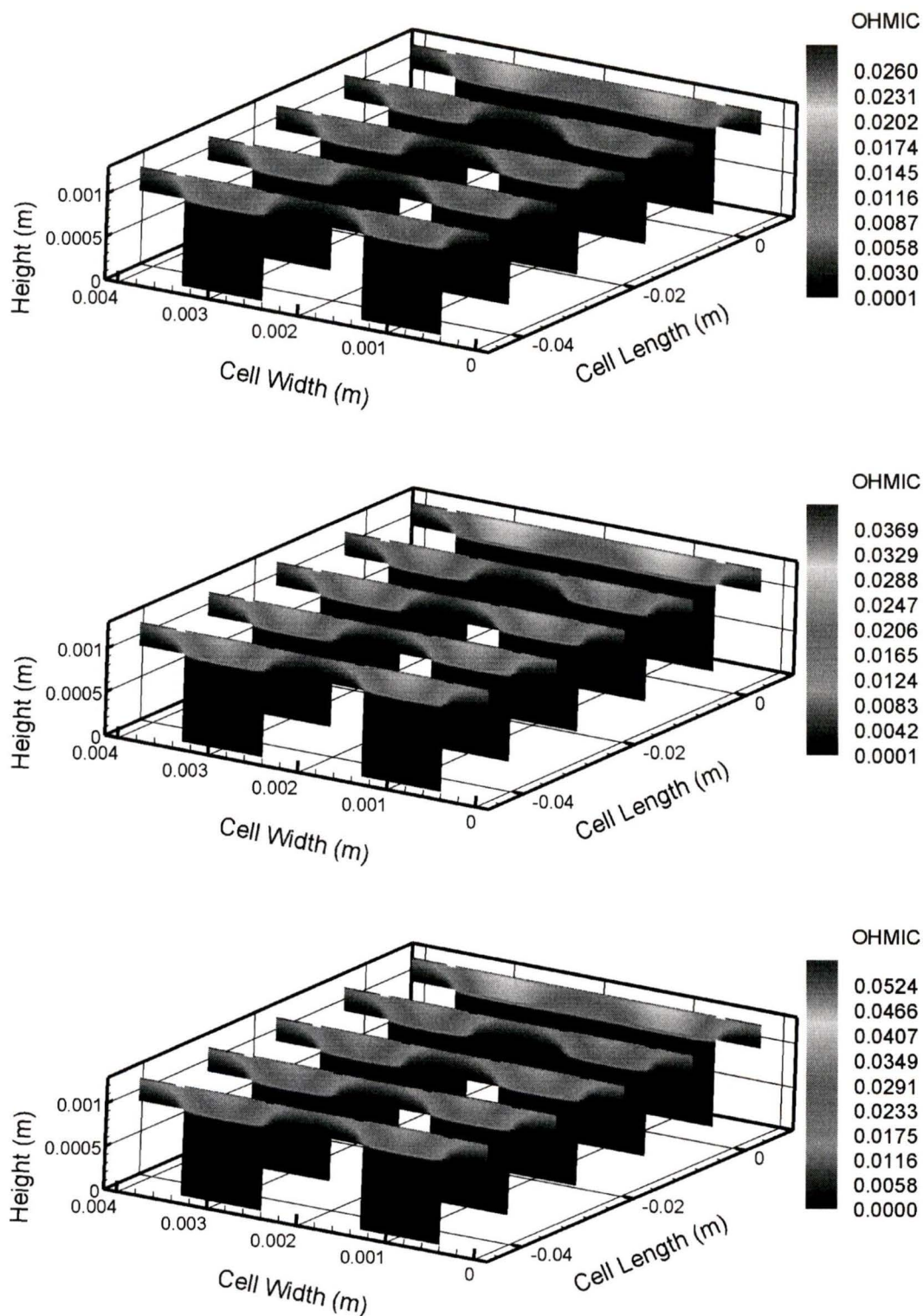


Figure 4.10. Ohmic overpotential in the cathode gas diffusion layer for three loading conditions: 0.3 A/cm² (top), 0.69 A/cm² (middle), and 1.2 A/cm² (bottom).

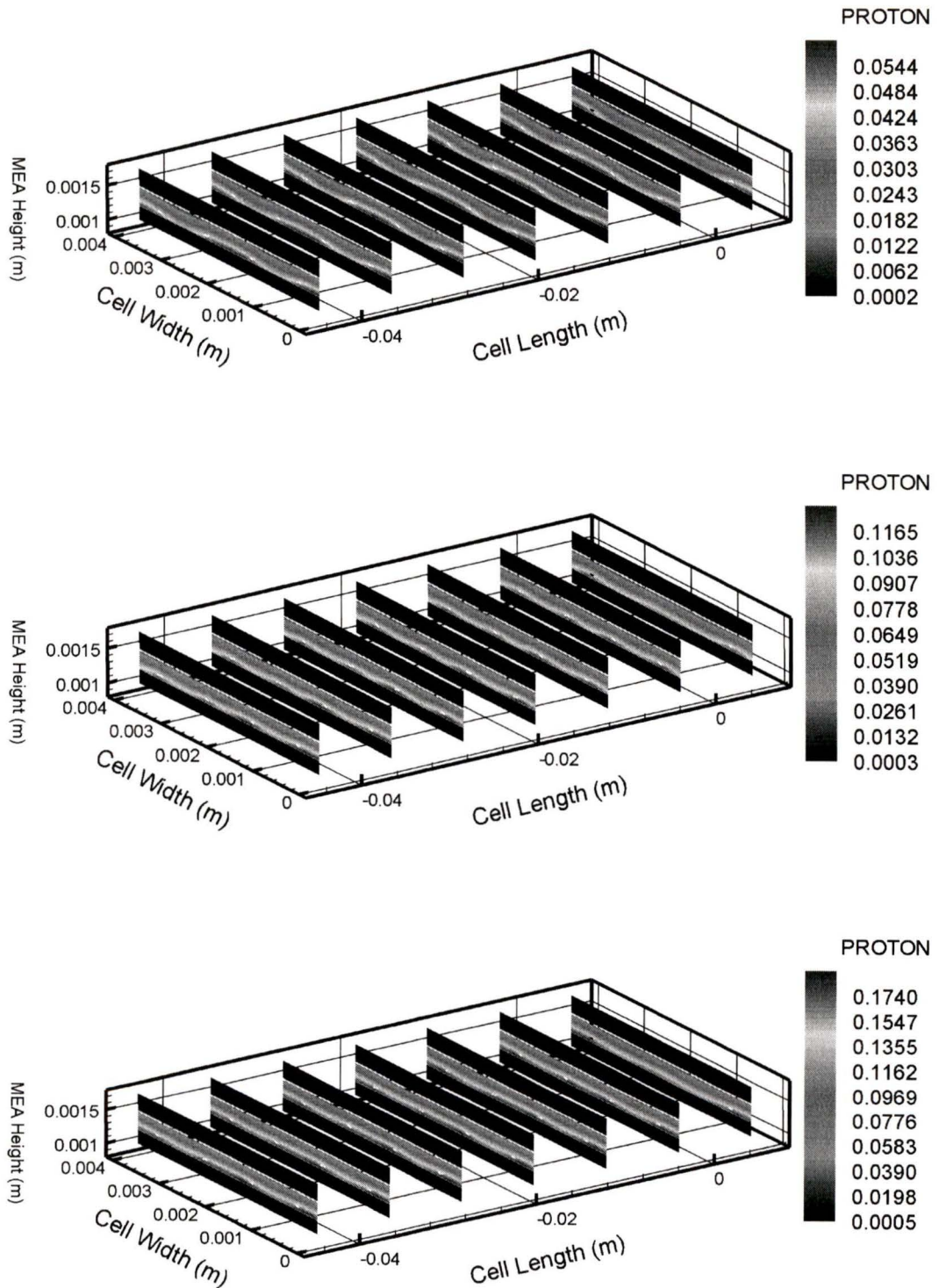


Figure 4.11. Potential drop across the membrane due to proton transport for three loading cases: 0.3 A/cm² (top), 0.69 A/cm² (middle), and 1.2 A/cm² (bottom).

4.2.8 Water Distribution in the Cell

The current model does not account for phase change, two-phase flow, and pore plugging by liquid water, but as a first assessment of the potential for flooding of the GDL, the water distribution in the cell is shown in Figure 4.12 as percent relative humidity. Significant condensation is expected to occur under the cathode land area for all loading conditions. However the magnitude for percent relative humidity is higher for high load condition than for low load condition. Also, under low load condition, the back diffusion is sufficient to counteract the electro-osmotic drag, but under high load condition the electro-osmotic effect dominates back diffusion. These phenomena result in a drier anode at higher load condition.

4.2.9 Cell Temperature Distribution

The temperature distribution inside the fuel cell is highly dependent on the loading conditions. It is assumed that all of the energy loss is converted to heat through electrochemical activation of the reactions or ohmic heating in the membrane and gas diffusion layers. However only electrochemical reaction heat generation at the cathode side is considered in this model since the activation is negligible in the anode side. Therefore the heat generation is highest in the region where the cathode electrochemical activity is highest.

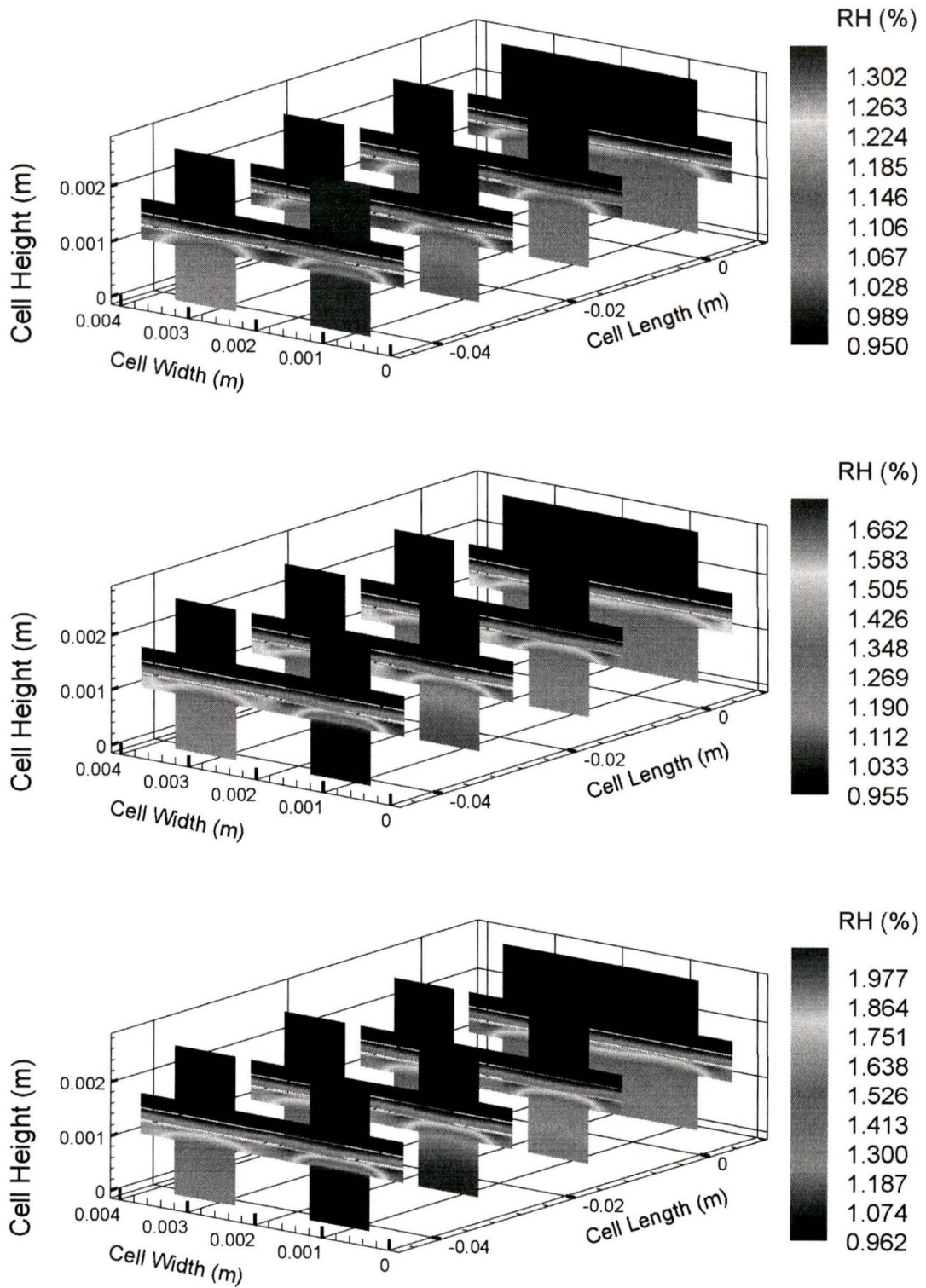


Figure 4.12. Water distribution in the cell for three different loading conditions: 0.3 A/cm² (top), 0.69 A/cm² (middle), and 1.2 A/cm² (bottom); (RH = relative humidity).

Temperature distribution for the intermediate and high load conditions are shown in Figure 4.13. In both cases the highest temperatures are located at the cathode catalyst layer. Since the membrane conductivity is quite low and there is no heat generation on the anode side, the anode side temperature is quite uniform and equals to the anode gas stream temperature. On the other hand the cathode gas temperature close to the channel gas diffusion layer interface is from 1 to 7 degrees higher than the nominal operating temperature.

4.2.10 Analysis of the Turning Region

Some interesting characteristics are observed at the turning region for the chosen geometry. The main cause of the different distribution patterns in the turning region is due to the higher ohmic loss in this region. This higher ohmic loss gives rise to a lower activation overpotentials which lead to lower current densities Figure 4.14. This higher ohmic loss in the turning region is due to the fact that the ohmic loss under the channel area is higher than under the land area and the main area of this region is under the channel area. This characteristic would not be observed if the gas diffusion layer is extended to cover the outside edge of the turning region.

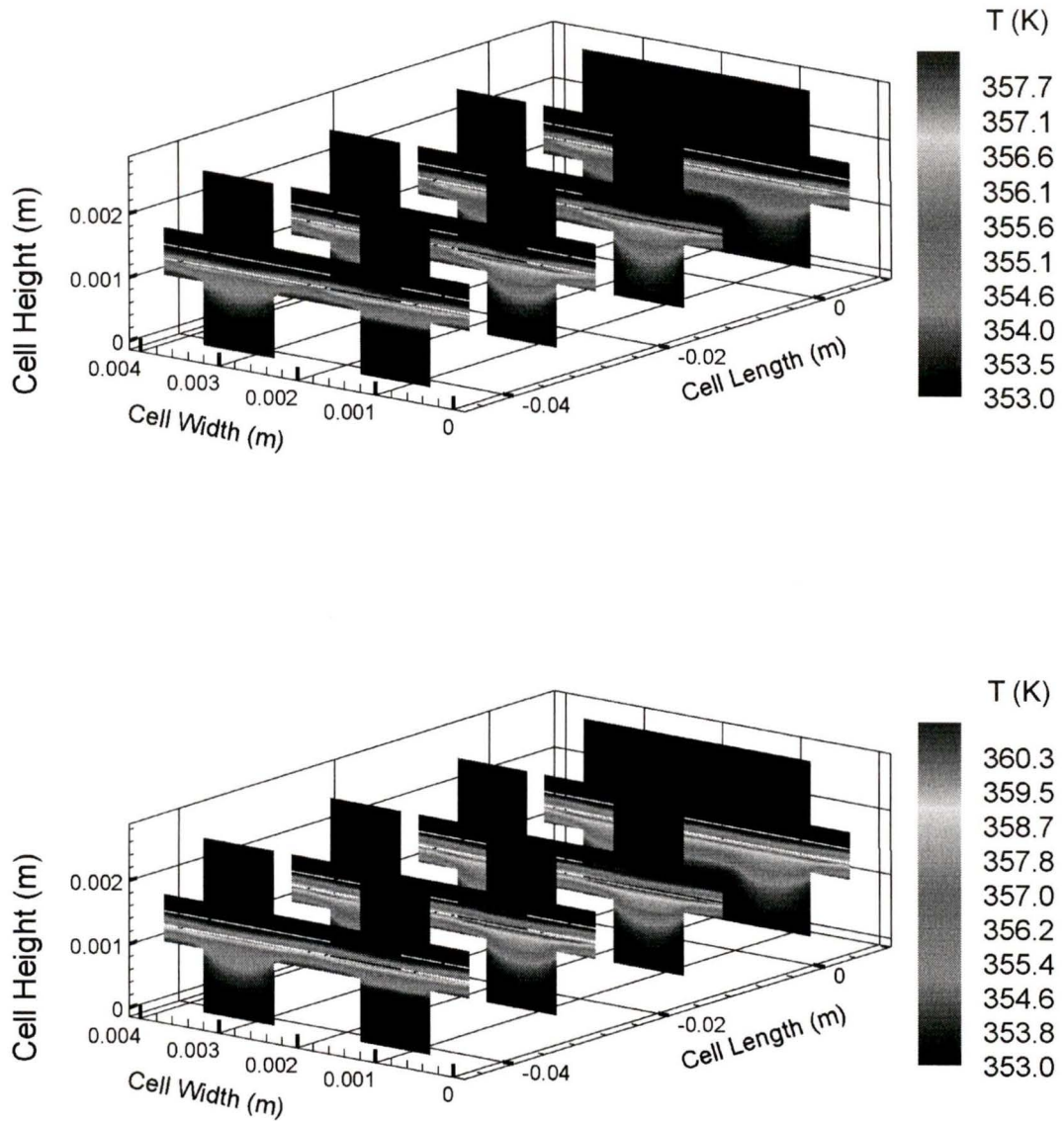


Figure 4.13. Temperature distribution in the cell for two loading cases: 0.69 A/cm^2 (top), and 1.2 A/cm^2 (bottom).

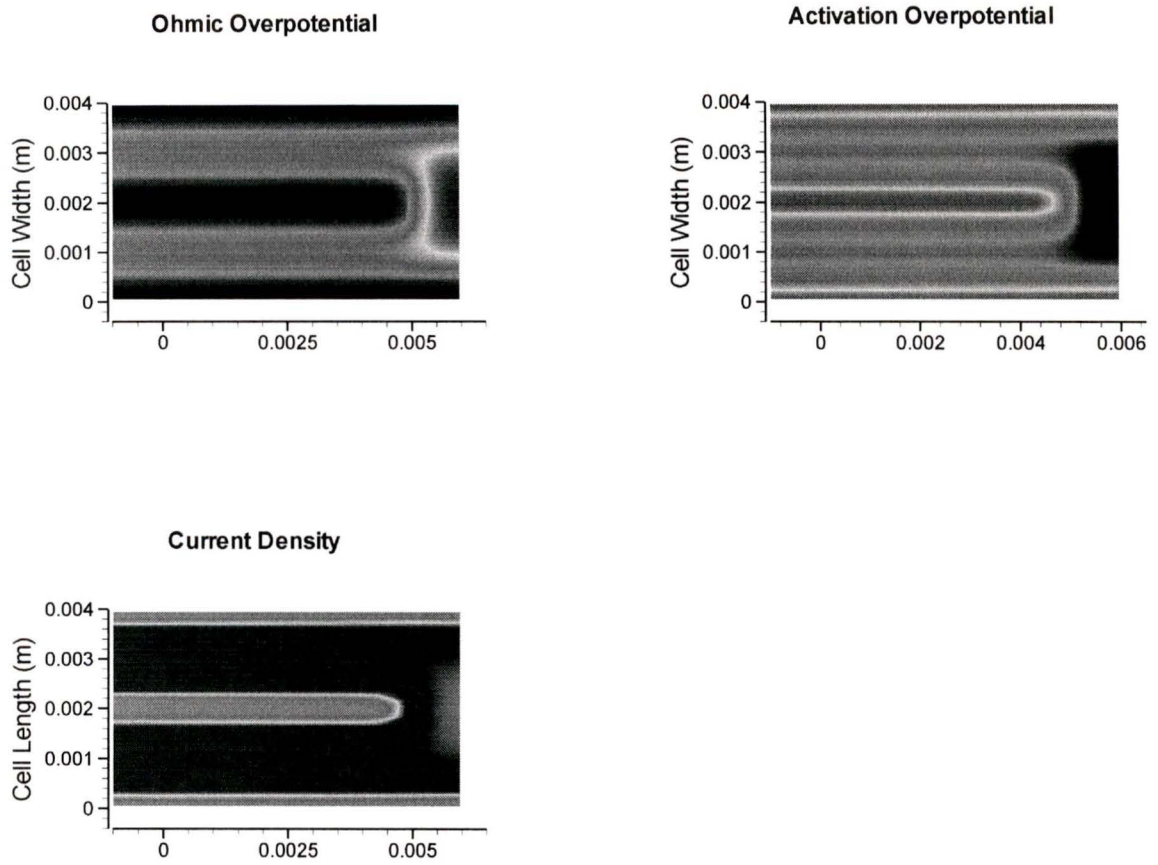


Figure 4.14. Distribution patterns at the turning region for the load of 1.2 A/cm^2 .

5 PARAMETRIC STUDY

In addition to revealing the detail of transport phenomena inside the fuel cell, a comprehensive three-dimensional model can also be used to investigate the sensitivity of certain parameters on fuel cell performance. The validated model is now ready for studying the effects of several operating and design parameters on fuel cell performance. The performance characteristics of the fuel cell based on a certain parameter can be obtained by varying that parameter while keeping all other parameters constant. Results obtained from these parametric studies will allow us to identify the critical parameters for fuel cell performance as well as the sensitivity of the model to these parameters. The fuel cell performance at various operating conditions is compared using the polarization curves, power curves, and assessment of other local distributions where appropriate.

5.1 Operating Parameters

Operating parameters are set during the operation of the fuel cell to give the desired output for a given application. The most important operating parameters are temperature, pressure, and stoichiometric flow ratio. The effects of these parameters on fuel cell performance are discussed in the following sections.

5.1.1 Effect of Temperature

Temperature change affects all transport phenomena and electrochemical kinetics inside the fuel cell. In this study, the pressure is kept constant at 3atm while the temperatures are varied from 323 K to 353 K. Temperature change requires the following

modifications to input conditions: exchange current density, reversible potential, membrane conductivity, inlet gas compositions, and gas diffusion coefficients.

The exchange current density, i_o^{ref} , is strongly dependent on temperature. The relationship between exchange current density and temperature has been studied experimentally by Parthasarathy et al. [33]. This empirical correlation will be used to calculate the appropriate exchange current density used for the model at different temperatures. Experimentally, the exchange current density can be obtained from the cyclic voltammograms of oxygen reduction. This method also allows us to calculate the reactive surface area of the catalyst layer and hence the roughness factor. Based on experimental results by Parthasarathy, the relationship between temperature and exchange current density is different for low current density and high current density because at low current density, some platinum oxide forms at the surface of the catalyst. However at high current density, platinum oxide formation disappears and the exchange current density is higher. In this model the relationship between exchange current density and temperature at higher current density is used because it resembles the activity of pure platinum catalyst surface.

The reference exchange current density (ai_o^{ref}) used for the base case was taken from Bernadi et al. [2]. This reference exchange current density used by Bernadi is actually the product of the active catalyst surface area per unit volume (cm^2/cm^3) and the exchange current density in A/cm^2 . Therefore this active surface area per unit volume can be calculated by comparing value given by Bernadi with the experimental value of reference exchange current density given by Partharsathy. The calculated active area per

unit volume is $a = 37.2 \text{ cm}^2/\text{cm}^3$. Applying this correction value to other temperatures, the exchange current densities at other temperatures can be obtained and listed in Table 5.1.

T (K)	i_o^{ref} (A/cm ²)	ai_o^{ref} (A/cm ³)
303	5.49281E-08	2.0455E-06
313	6.29208E-08	2.3431E-06
323	9.99878E-08	3.7235E-06
333	1.37055E-07	5.1039E-06
343	2.12224E-07	7.9031E-06
353	2.68531E-07	1.0E-05

Table 5.1. Variation of exchange current density with temperatures at 3atm.

The reversible potential decreases with increasing temperatures because the Gibbs free energy change of the reaction decreases with temperature increase. The reversible potentials at various temperatures at 3atm are listed in Table 5.2. The membrane conductivity is also dependent on temperature. The empirical relation of membrane conductivity and temperature used to calculate membrane conductivities at various temperatures was given by Springer et al. [37]. The calculated values are shown in Table 5.2.

T (K)	E_{rev} (V)	σ (Scm ⁻¹)
323	1.209	0.1455
333	1.198	0.1510
343	1.187	0.1566
353	1.176	0.1760
363	1.164	0.1926

Table 5.2. Variation of cell reversible potentials and membrane conductivity with temperatures.

The gas compositions of the inlet gas streams are also affected by temperature since saturation pressure is a function of temperature. Therefore, the molar fraction of water vapor in fully humidified gas streams increases with temperature for a fixed total pressure. On the other hand, the molar fractions of oxygen and nitrogen decreases with increasing temperature in a fully humidified inlet stream with constant total pressure.

Given,

$$X_{H_2O,in} = \frac{P_{sat}(T)}{P_{in}} \quad (5.1)$$

and assuming the ratio of nitrogen to oxygen in dry air (79:21) does not change with temperature, the molar fraction of oxygen can be obtained as follow:

$$X_{O_2,in} = \frac{1 - X_{H_2O,in}}{1 + \frac{79}{21}} \quad (5.2)$$

Since the sum of all molar fractions is unity, the molar fraction of nitrogen can be obtained:

$$X_{N_2,in} = 1 - X_{H_2O,in} + X_{O_2,in} \quad (5.3)$$

Figure 5.1 shows a plot of molar fractions versus temperatures for the gas compositions of the cathode inlet stream. The gas composition of the anode inlet stream is much simpler since there are only two gas species, hydrogen and water vapor. The molar fraction of hydrogen is determined from the unity relation as follow:

$$X_{H_2,in} = 1 - X_{H_2O,in} \quad (5.4)$$

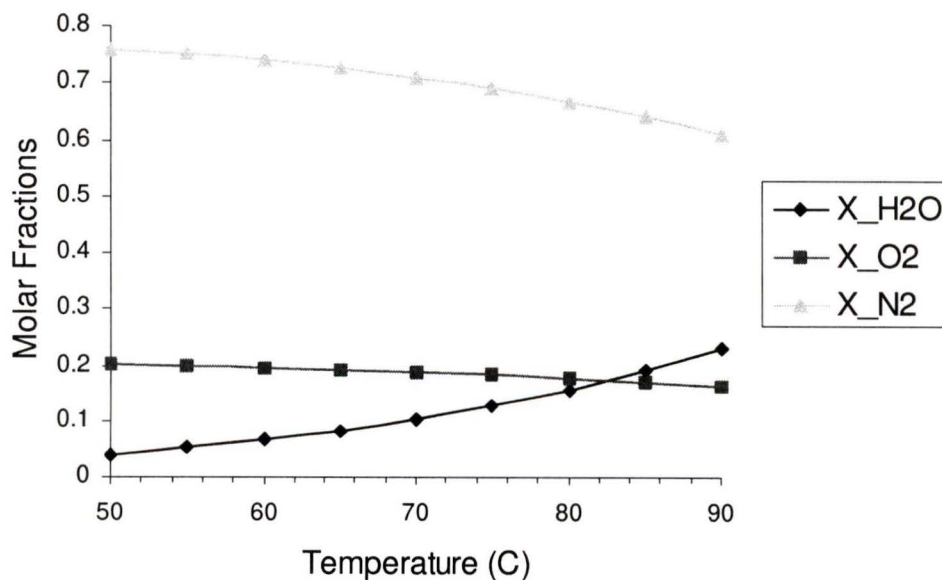


Figure 5.1. Fully humidified inlet air compositions at different temperatures.

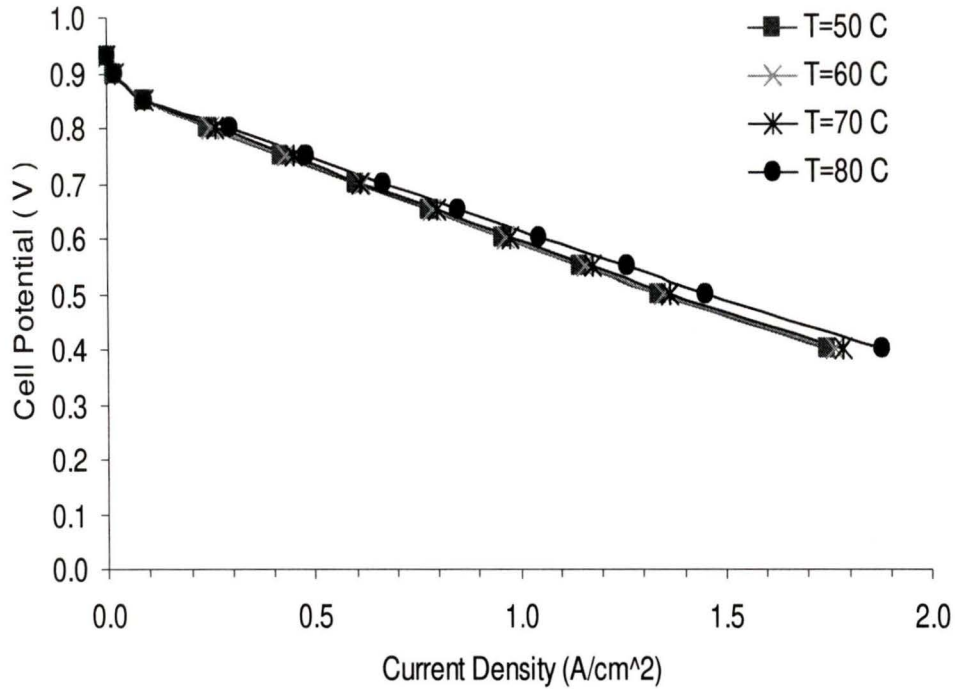


Figure 5.2. Effect of temperature on fuel cell performance.

The polarization curves of the cell at different operating temperatures show that fuel cell performance is improved with increasing temperatures. This is in agreement with experimental parametric study [40]. Generally the performance is better in all regions along the polarization curve however the gain is larger in the ohmic loss region than the activation overpotential loss region. This observation could be explained by the increase in gas diffusivity and membrane conductivity at higher temperature.

5.1.2 Effect of Pressure

Pressure is another operating parameter that has large effects on fuel cell performance. The following input parameters need to be changed with pressure change, inlet gas compositions, exchange current density, reversible electrode potential, and the diffusivities of the binary diffusion coefficients.

In this parametric study, the cell operating temperature is kept at 353 K, while the pressure is varied from 1 atm to 5 atm. Since the saturation pressure remains constant for constant operating temperature, the molar fraction of water vapor decreases with increasing total pressure. The molar fraction of oxygen increases with increasing operating pressure. Figure 5.3 shows the variation of inlet gas compositions with pressures.

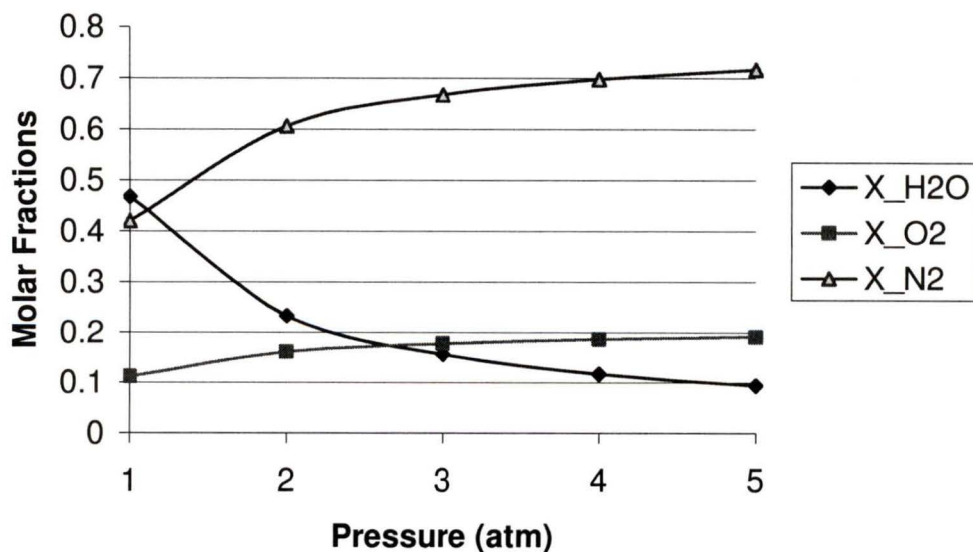


Figure 5.3. Fully humidified inlet air compositions at different pressures.

The relationship between exchange current density and pressure was investigated by Parthasarathy et al. [34]. This relationship was used to calculate the exchange current density at various pressures used in this parametric study. The experimental exchange current densities were obtained at 50°C, and the parametric studies are done at 80°C, therefore the exchange current densities used in this study must be adjusted for temperature. A correction factor was obtained by dividing the exchange current density at 80°C by the exchange current density at 50°C. This correction factor was then applied to all exchange current densities at various oxygen partial pressures. The exchange current densities used in this study was then interpolated from the newly adjusted values. The exchange current densities used in this study are listed in Table 5.3. The cell reversible potential also increases slightly with pressure as the activity of oxygen is increased with increasing pressures. The reversible potentials at different pressures are also shown in Table 5.3.

P_c (atm)	P_{O_2} (atm)	ai_o^{ref} (A/cm ³)	E_{rev} (V)
1	0.1117824	4.7823E-06	1.1739
2	0.3217824	6.2592E-06	1.1751
3	0.5317824	0.00001	1.1758
4	0.7417824	1.5655E-05	1.1763
5	0.9517824	2.351E-05	1.1767

Table 5.3. Variation of exchange current density and reversible potential with pressures.

The polarization curves of different cell operating pressures are shown in Figure 5.4. As the operating pressure is increased from 1 atm to 5 atm, the fuel cell performance also increases. This performance behavior was also observed in the experimental study by Wang et al. [40]. The performance gain is gradual in the region from 1 atm to 3 atm but the gain diminishes as the pressure is increased above 4 atm.

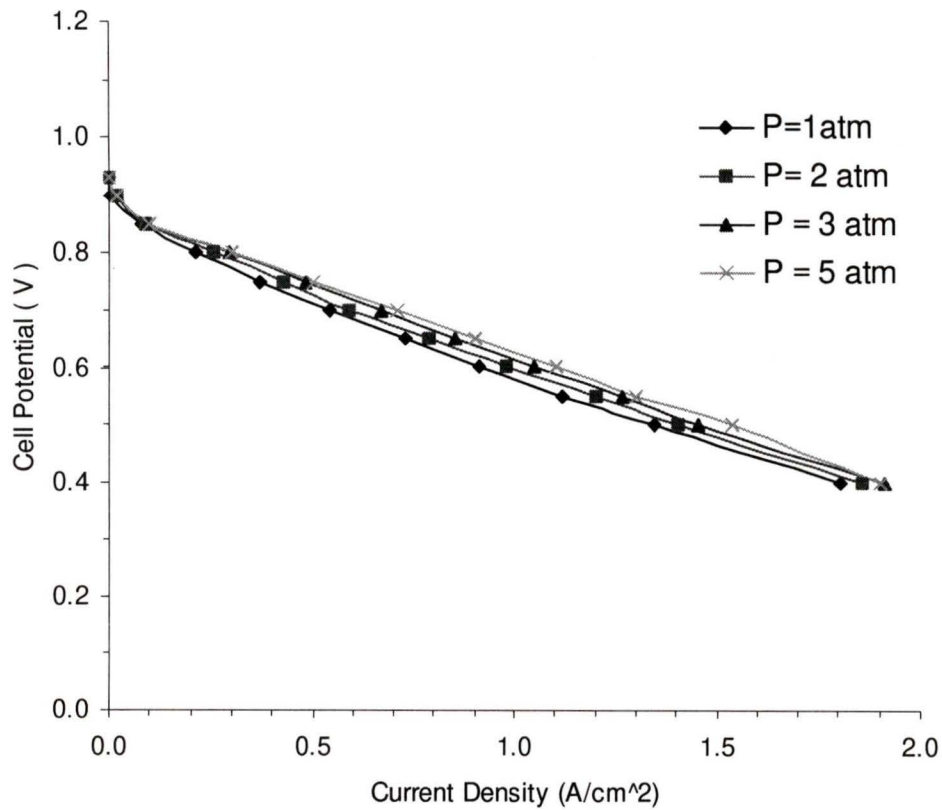


Figure 5.4. Effect of pressure on fuel cell performance

5.2 Design Parameters and Material Properties

5.2.1 Effect of Electrode Porosity

The porosity of the gas diffusion layers can affect the performance of the fuel cell in two ways. First the electrode porosity affects the mass transport of reactant gases from the channel towards the catalyst layers, with higher volume porosity providing less resistance to mass transport. The volume porosity also affects the gas diffusion coefficients through the Bruggemann correction. Second, the electrode porosity has a negative effect on electron conduction, since the solid matrix of the gas diffusion layer provide the pathways for electron transport, the higher volume porosity increases resistance to electron transport in the gas diffusion layers.

The simulation results of the effects of electrode porosity on fuel cell performance are shown in Figure 5.5 for three different electrode porosities of 0.3, 0.4, and 0.5. It is evident from this figure that the fuel cell performs better at higher electrode porosity. The gain in performance is greater in the high load region compared to the low load region.

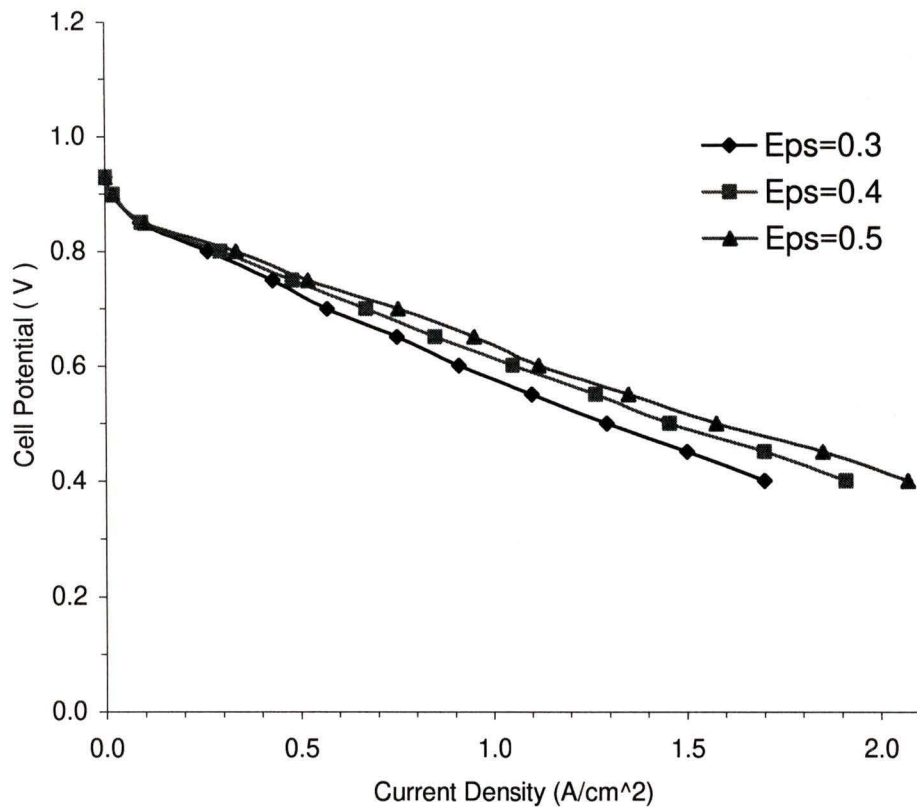


Figure 5.5. Polarization curves illustrating the effect of electrode porosity on fuel cell performance.

6 CONCLUSIONS AND RECOMMENDATIONS

6.1 Conclusions

A three-dimensional computational fluid dynamics model of PEM fuel cell with serpentine flow channels was developed in this work. This model provides valuable information about the transport phenomena inside the fuel cell such as reactant gas concentration distribution, temperature distribution, potential distribution in the membrane and gas diffusion layers, activation overpotential distribution, and local current density distribution.

The unique feature of this model is the implementation of the voltage-to-current (VTC) algorithm that allows for the calculation of the electrochemical kinetics without simplifications. This calculation involves the coupling of the potential field with the reactant species concentration field which results in an accurate prediction of local current density distribution. Furthermore, the current density distribution patterns vary with loading conditions. At low load, the current density is higher in the land area and as the load is increased, the current density maxima shifts towards the center of the channel. These local current density distribution patterns are radically different from those obtained with models that do not account for the non-uniformity of surface overpotential. In addition, the three-dimensional activity of the catalyst layer is also accounted for in this model. The results show that at moderate and high load conditions, most of the activity occurs at the first catalyst sub-layer adjacent to the GDL.

In addition to revealing the detail information about the transport phenomena inside the fuel cell, this model was applied to investigate the sensitivity of various operating and

material parameters on fuel cell performance. The results of these studies show that fuel cell perform better at higher temperature, pressure, and electrode porosity.

6.2 Contributions

Two main contributions were made during the course of this thesis work:

- i. The development and implementation of the voltage-to-current (VTC) algorithm that accounts for the accurate prediction of the current density distribution through the coupling of varying activation overpotential with local reactant concentrations.
- ii. The implementation of serpentine gas flow channels instead of straight channels.

6.3 Recommendations

Generally, the results obtained from this model are in agreement with experimental results. However, there are still a number of limitations to be addressed to improve this model further.

- i. A major limitation is the over estimate of current in the mass transport region of the polarization curve. This limitation can be improved by including two-phase flow in the model to account for flooding effects at high loads.
- ii. Improvement of the membrane model to account for the dependence of electro-osmotic drag coefficient and protonic conductivity with membrane water content.

- iii. Expansion of the computational domain from one serpentine turn to a single cell that has many turns. This would be very computationally demanding and would require a code that can support parallel processing.
- iv. Extension of the model from steady state to transient.

APPENDIX A

MULTICOMPONENT DIFFUSION COEFFICIENT

This section summarizes the steps used in estimating the ternary component diffusion coefficients given by Taylor and Krishna [38].

The Maxwell-Stefan equations are derived by considering the conservation of momentum for an elastic collision. The form is given as,

$$\nabla x_i = \sum_{j=1}^{n-1} \frac{x_i x_j}{D_{ij}} (\mathbf{v}_j - \mathbf{v}_i) \quad (\text{A. 1})$$

where D_{ij} are the binary diffusion coefficients. Eliminating the velocities using the definition of the molar fluxes $\vec{N}_i = c_i \vec{v}_i$,

$$\nabla x_i = \sum_{j=1}^{n-1} \frac{1}{c_i D_{ij}} (x_i \vec{N}_j - x_j \vec{N}_i) \quad (\text{A. 2})$$

or, in terms of the diffusion fluxes J_i

$$\nabla x_i = \sum_{j=1}^{n-1} \frac{1}{c_i D_{ij}} (x_i \vec{J}_j - x_j \vec{J}_i) \quad (\text{A. 3})$$

The above equation can be rewritten by eliminating one flux component,

$$c_i \nabla x_i = -B_{ii} \vec{J}_i - \sum_{\substack{j=1 \\ j \neq i}}^{n-1} B_{ij} \vec{J}_j \quad (\text{A. 4})$$

where the coefficients B_{ii} and B_{ij} are defined as,

$$B_{ii} = \frac{x_i}{D_{in}} + \sum_{\substack{j=1 \\ j \neq i}}^{n-1} \frac{x_j}{D_{ij}} \quad (\text{A. 5})$$

$$B_{ij} = -x_i \left(\frac{1}{D_{ij}} - \frac{1}{D_{in}} \right) \quad (\text{A. 6})$$

Now the $(n-1)$ equations of the form (4) can be written in $(n-1)$ dimensional matrix form as:

$$c_t(\nabla x_i) = -[B](J) \quad (\text{A. 7})$$

where $[B]$ is a square matrix of order $n-1$.

$$[B] \equiv \begin{bmatrix} B_{1,1} & B_{1,2} & \dots & B_{1,n-1} \\ B_{2,1} & B_{11} & & \vdots \\ \vdots & & & \vdots \\ B_{n-1,1} & \dots & \dots & B_{n-1,n-1} \end{bmatrix} \quad (\text{A. 8})$$

The column matrix (J) is

$$(J) = \begin{pmatrix} J_1 \\ J_2 \\ \vdots \\ J_{n-1} \end{pmatrix} \quad (\text{A. 9})$$

and (∇x_i) is a column matrix of order $n-1$ given by:

$$(\nabla x_i) = \begin{pmatrix} \nabla x_1 \\ \nabla x_2 \\ \vdots \\ \nabla x_{n-1} \end{pmatrix} \quad (\text{A. 10})$$

This can be rewritten as an equation for the diffusive flux as:

$$(J) = -c_t[B]^{-1}(\nabla x_i) \quad (\text{A. 11})$$

The common form of multi-component mass transport equations are usually given in Fick's Law as,

$$\vec{J}_1 = -c_t D_{11} \nabla x_1 - c_t D_{12} \nabla x_2 \quad (\text{A. 12})$$

$$\vec{J}_2 = -c_t D_{21} \nabla x_1 - c_t D_{22} \nabla x_2 \quad (\text{A. 13})$$

Only two fluxes (\vec{J}_1, \vec{J}_2) and two driving forces $(\nabla x_1, \nabla x_2)$ in a ternary mixture are independent. The diffusion coefficients in the above equations are multi-species diffusion coefficients; note that four of them are needed to characterize a ternary system. These coefficients are not to be confused with the binary diffusion coefficients; they may take positive or negative signs and they are not, in general, symmetric ($D_{ij} \neq D_{ji}$). The matrix representation of the generalized Fick's law is as follows:

$$(J) = -c_t [D] (\nabla x) \quad (\text{A. 14})$$

Alternative forms of the Generalized Fick's law are given in chapter 3.2.2:

Molar flux with respect to the molar average velocity:

$$(J) = -c_t [D] (\nabla x) \quad (\text{A. 15})$$

Mass flux with respect to the mass average velocity:

$$(j) = -\rho_t [D^0] (\nabla w) \quad (\text{A. 16})$$

Molar flux with respect to volume average velocity:

$$(J^v) = -[D^v] (\nabla c) \quad (\text{A. 17})$$

Comparison of the Maxwell-Stefan formulation

$$(J) = -c_t [B]^{-1} (\nabla x) \quad (\text{A. 18})$$

with the generalized Fick's law:

$$(J) = -c_t [D] (\nabla x) \quad (\text{A. 19})$$

shows that the matrix $[D]$ and the product $[B]^{-1}$ are equivalent

$$[D] = [B]^{-1} \quad (\text{A. 20})$$

Therefore for a ternary mixture, the diffusion coefficients can be calculated as follows:

Calculating components of matrix [B],

$$B_{11} = \frac{x_1}{d_{13}} + \frac{x_2}{d_{12}} + \frac{x_3}{d_{13}}$$

$$B_{12} = -x_1 \left(\frac{1}{d_{12}} - \frac{1}{d_{13}} \right)$$

$$B_{21} = -x_2 \left(\frac{1}{d_{12}} - \frac{1}{d_{23}} \right)$$

$$B_{22} = \frac{x_1}{d_{12}} + \frac{x_2}{d_{23}} + \frac{x_3}{d_{23}}$$

(A. 21)

Matrix [D] is the inverse of [B].

REFERENCES

- [1] F. Barbir, J. Braun, and J. Neutzler. "Properties of Molded Graphite Bi-Polar Plates for PEM Fuel Cell Stacks", *Journal of New materials for Electrochemical Systems*, 2:197-200, 1999.
- [2] D.M. Bernardi and M.W. Verbrugge. "Mathematical Model of a Gas Diffusion Electrode Bonded to a Polymer Electrolyte". *AIChE Journal*, 37(8): 1151-1162, 1991.
- [3] D. M. Bernadi and M. W. Verbrugge. "A Mathematical Model of the Solid-Polymer-Electrolyte Fuel Cell". *J. Electrochem. Soc.*, 139(9): 2477-2491, 1992.
- [4] T. Berning "Three-Dimensional Computational Analysis of Transport Phenomena in a PEM Fuel Cell". PhD Thesis, 2002.
- [5] T. Berning, D.M. Lu, N. Djilali. "Three-Dimensional Computational Analysis of Transport Phenomena in a PEM Fuel Cell". *Journal of Power Sources*, 106: 284-294, 2002.
- [6] R.B. Bird, W. Stewart, and E. N. Lightfoot. "Transport Phenomena". Wiley, New York, 1960.
- [7] F.N. Buchi, and S. Srinivasan. "Operating Proton Exchange Membrane Fuel Cells Without External Humidification of the Reactant Gases". *J. Electrochem. Soc.*, 144(8): 2767-2772, 1997.
- [8] S. Chintada, K-H Ko, and N. K. Anand. "Heat Transfer in 3-D Serpentine Channels with right-Angle Turns". *Numerical Heat Transfer, Part A*, Vol. 36, 781-806, 1999.
- [9] J.M. Choi and N.K. Anand. "Heat Transfer in a Serpentine Channel with a Series of Right-Angle Turns". *Numerical Heat Transfer, Part A*, Vol. 23, 189-210, 1993.
- [10] E.L. Cussler. "Diffusion-Mass Transfer in Fluid Systems". Cambridge University Press, 1984.
- [11] S. Dutta, S. Shimpalee, J.W. Van Zee. "Three-dimensional numerical simulation of straight channel PEM fuel cells". *Journal of Applied Electrochemistry*, Vol. 30, 135-146, 2000.
- [12] S. Dutta, S. Shimpalee, J.W. Van Zee. "Numerical Prediction of Mass-Exchange Between Cathode and Anode Channels in a PEM Fuel Cell". *International Journal of Heat and Mass Transfer*, 44:2029-2042, 2001.

- [13] M. Eikerling, and A.A. Kornyshev. "Proton transfer in a single pore of a polymer electrolyte membrane". *J. Electroanalytical Chemistry*, Vol. 502, 1-14, 2001.
- [14] M. Eikerling, A.A. Kornyshev, A.M. Kuznetsov, J.Ulstrup, and S.Walbran "Mechanism of Proton Conductance in Polymer Electrolyte Membranes". *J. Phys. Chem. B*, Vol. 105, 3646-4662, 2001.
- [15] J.H. Ferziger and M. Peric. "Computational Methods for Fluid Dynamics". Springer, 1997.
- [16] T.F. Fuller and J. Newman. "Water and Thermal Management in Solid-Polymer-Electrolyte Fuel Cells". *J. Electrochem. Soc.*, 140(5):1218-1225, 1993.
- [17] S. Gamburgzev and A.J. Appleby. "Recent Progress in Performance Improvement of the Proton Exchange Membrane Fuel Cell (PEMFC)". *Journal of Power Sources*, 107:5-12, 2002.
- [18] T.D. Gierke, G.E. Munn, and F.C. Wilson. "The Morphology in Nafion Perfluorinated Membrane Products, as Determined by Wide- and Small-Angle X-Ray Studies". *J. Polymer Science, Polymer physics edition*, Vol. 19, 1687-1704, 1981.
- [19] V. Gurau, F. Barbir, and H. Liu. "An Analytical Solution of a Half-Cell Model for PEM Fuel Cells". *J. Electrochem. Soc.*, 147(7): 2468-2477, 2000.
- [20] V. Gurau, H. Liu, and S. Kakac. "Two-Dimensional Model for Proton Exchange Membrane Fuel Cells". *AIChE Journal*, 44(11): 2410-2421, 1998.
- [21] W.Y. Hsu and T.D. Gierke. "Ion Transport and Clustering in Nafion Perfluorinated Membranes". *J. Membrane Science*, Vol. 13, 307-326, 1983.
- [22] J.-J. Hwang and D.-Y. Lai. "Three-Dimensional laminar Flow in a Rotating Multiple-Pass Square Channel with Sharp 180-Deg Turns". *Transactions of the ASME*, Vol. 120, 488-495, 1998.
- [23] F.P. Incropera and D.P. DeWitt. "Fundamentals of Heat and Mass Transfer". John Wiley & Sons, 4th Edition, 1996.
- [24] A. Kumar and R.G. Reddy. "Effect of channel dimensions and shape in the flow-field distributor on the performance of polymer electrolyte membrane fuel cells". *Journal of Power Sources*, Vol. 113, 11-18, 2003.
- [25] J. Laminie and A. Dicks. "Fuel Cell Systems Explained". Wiley, 2000.

- [26] M. J. Lampinen and M. Fomino. "Analysis of Free Energy and Entropy Changes for Half-Cell Reactions". *J. Electrochem. Soc.*, 140(12): 3537-3546, 1993.
- [27] M. Mehta, and J. S. Cooper. "Review and analysis of PEM fuel cell design and manufacturing". *Journal of Power Sources*, 114:32-53, 2003.
- [28] J.S. Newman "Electrochemical Systems". Prentice Hall, 2nd Edition, 1991.
- [29] T. V. Nguyen and R. E. White. "A Water and Heat Management Model for Proton-Exchange-Membrane Fuel Cells". *J. Electrochem. Soc.*, 140(8): 2178-2186, 1993.
- [30] R.C. Nickerson "Fundamentals of Fortran Programming". Second Edition, 1980.
- [31] D.A. Nield and A. Bejan. "Convection in Porous Media". Springer, 2nd Edition, 1999.
- [32] H.B. Oldham and J.C. Myland . "Fundamentals of Electrochemical Science". Academic Press, 1994.
- [33] A. Parthasarathy, S. Srinivasan, A. J. Appleby and C. R. Martin "Temperature Dependence of the Electrode Kinetics of Oxygen Reduction at the Platinum/Nafion Interface-A Microelectrode Investigation". *J. Electrochem. Soc.*, 139(9): 2530-2537, 1992.
- [34] A. Parthasarathy, S. Srinivasan, A. J. Appleby, and C. R. Martin. "Pressure Dependence of the Oxygen Reduction Reaction at the Platinum Microelectrode/Nafion Interface: Electrode Kinetics and Mass Transport". *J. Electrochem. Soc.*, 139(10): 2856-2862, 1992.
- [35] S.V. Patankar, C.H. Liu, and E.M. Sparrow. "Fully Developed Flow and Heat Transfer in Ducts Having Streamwise-Periodic Variations Cross-Sectional Area". *Transactions of the ASME*, Vol. 99, 180-185, 1977.
- [36] N.P. Siegel, M.W. Ellis, D.J. Nelson, and M.R. von Spakovsky. "Single Domain PEMFC model based on agglomerate catalyst geometry". *Journal of Power Sources*, Vol. 5095, 1-9, 2002.
- [37] T.E. Springer, T.A. Zawodzinski, and S. Gottesfeld. "Polymer Electrolyte Fuel Cell Model". *J. Electrochem. Soc.*, 138(8): 2334-2342, 1991.
- [38] R. Taylor and R. Krishna. "Multicomponent Mass Transfer". John Wiley & Sons, 1993.

- [39] S. Um, C.-Y. Wang, and K.S. Chen. "Computational Fluid Dynamics Modeling of Proton Exchange Membrane Fuel Cells". *J. Electrochem. Soc.*, 147(12): 4485-4493, 2000.
- [40] L Wang, A. Husar, T. Zhou, H. Liu. "A Parametric Study of PEM Fuel Cell Performances". *International Journal of Hydrogen Energy*, 28: 1263-1272, 2003.
- [41] Z. H. Wang, C. Y. Wang and K. S. Chen, "Two-Phase Flow and Transport in the Air Cathode of Proton Exchange Membrane Fuel Cells", *J. Power Sources*, 94(1): 40-50, 2001.
- [42] L You and H. Liu. "A Parametric Study of the Cathode Catalyst Layer of PEM Fuel Cells Using a Pseudo-Homogenous Model". *International Journal of Hydrogen Energy*, 26: 991-999, 2001.
- [43] T. A. Zawodzinski, C. Derouin, S. Radzinski, R.J. Sherman, V.T. Smith, T.E. Springer, and S. Gottesfeld. "Water Uptake by and Transport Through Nafion 117 Membranes". *J. Electrochem. Soc.*, 140(4): 1041-1337, 1993.

VITA

Surname: Nguyen

Given Names: Phong Thanh

Place of Birth: Ho Chi Minh City, Vietnam

Educational Institutions Attended:

University of Victoria	2001 – 2003
University of Western Ontario	1996 – 2001

Degrees Awarded:

B.E.Sc.	University of Western Ontario	2001
---------	-------------------------------	------

Honours and Awards:

BC Advanced Systems Institute (ASI) communication award	2003
University of Victoria Fellowship	2001

Publications:

P. T. Nguyen, T. Berning, M. Bang, N. Djilali. "A Three-Dimensional Model of PEM Fuel Cell with Serpentine Flow Channels". Hydrogen and Fuel Cells conference proceedings, 2003.

UNIVERSITY OF VICTORIA PARTIAL COPYRIGHT LICENSE

I hereby grant the right to lend my thesis (or dissertation) to users of the University of Victoria Library, and to make single copies only for such users or in response to a request from the Library of any other university, or similar institution, on its behalf or for one of its users. I further agree that permission for extensive copying of this thesis for scholarly purposes may be granted by me or a member of the University designated by me. It is understood that copying or publication of this thesis for financial gain by the University of Victoria shall not be allowed without my written permission.

Thesis Title:

A Three-Dimensional Computational Model of PEM Fuel Cell with Serpentine Gas Channels

Author

Phong Thanh Nguyen
September 15, 2003